Supplementary Material

For “Genetic Analysis of Right Heart Structure and Function in 40,000 People”.

Supplementary Note

Supplementary Results

Deep learning quality assessment and inter-rater reliability

The four-chamber long axis deep learning model output was compared to a randomly chosen held-out test set of 40 additional manually annotated images (by two annotators: JPP and VN) that were not used for training or validation. The Dice coefficients for the right atrial and right ventricular blood pools between the annotators and the model were uniformly high—above 0.90 on average with low variance (standard deviation ranging from 0.03-0.04) (**Supplementary Table 14**).

The short axis deep learning model output was first assessed against 57 test set images (manually annotated by JPP). The average Dice coefficient of the deep learning model output was 0.89 ± 0.21 (representing mean ± standard deviation [SD]) for the right ventricular blood pool and 0.96 ± 0.16 for the pulmonary artery blood pool. From those values, we observed that, despite similar point estimates, the short axis measurements had greater variance in their Dice scores compared to the four-chamber long axis measurements, despite the short axis model having more training data.

We then had three experts (JPP, VN, and JC) annotate 50 randomly chosen held-out short axis images that were not used to train the deep learning model. Dice scores for the short axis right ventricular blood pool among the three raters ranged from 0.80-0.87, those for the pulmonary artery ranged from 0.76-0.82, and those for the left ventricular blood pool ranged from 0.75-0.89 (**Supplementary Tables 15-17**). The annotators' agreements with the deep learning model output ranged from Dice 0.79-0.90 for the RV, 0.71-0.81 for the PA, and 0.83-0.93 for the LV.

Across all comparisons, we observed the same pattern of high Dice score standard deviation for short axis annotations when compared to the same structure being annotated in the four-chamber view. We looked at properties of all available images on which the deep learning models were successfully applied (24,378,930 short axis images and 2,296,549 four-chamber long axis images). On average, the short axis images contained 39,600 ± 4,500 pixels, whereas the four-chamber long axis images contained 35,200 ± 3,700 pixels. This yielded a larger coefficient of variation (standard deviation divided by mean) for the number of pixels in short axis images than in four-chamber long axis images (0.114 vs 0.105). In addition, the portion of each image occupied by the structures of interest was smaller in the short axis images than in the four-chamber long axis images. The right ventricular blood pool was measured in both views and offers a direct comparison: 0.68±0.79% of pixels in the short axis and 1.78±0.53% of pixels in the four-chamber long axis view were annotated as belonging to the right ventricle. We concluded that both (a) the portion of the image occupied by structures of interest (0.68% for short axis vs 1.78% for four-chamber long axis), and (b) the variability of how much of the image is occupied by those structures (coefficient of variation 1.16 for short axis and 0.30 for four-

chamber long axis) likely contribute to the greater variation in Dice score for the annotated structures of the short axis images. Of note, when the Dice scores were weighted by the total number of pixels attributed to the RV (represented by the “Weighted Dice” columns in **Supplementary Tables 15-17**), we found that the variance was lower, consistent with greater agreement in the images that ultimately contribute more pixels to the RV estimates in the downstream Poisson reconstruction models.

Measurement of right heart structures

The right atrium was only consistently visible in one view (the four-chamber long axis view), and therefore a 2-dimensional area was computed by summing the pixels and multiplying by their width and height. We computed the maximum and minimum area during the cardiac cycle, as well as the fractional area change (RA FAC), which is the ratio of the change in area between the maximum and minimum area divided by the maximum area.

The right ventricle has a complex 3-dimensional geometry; to estimate right ventricular structure, we integrated data from the short axis views and the four-chamber long axis view with a Poisson surface reconstruction approach, detailed in the **Supplementary Methods**. We measured the maximum volume (right ventricular end diastolic volume; RVEDV), the minimum volume (right ventricular end systolic volume; RVESV), the difference between those two volumes (stroke volume), and the ejection fraction (RVEF).

The pulmonary trunk’s elliptical minor axis (diameter) was computed from short axis images[1,2]. For participants whose pulmonary trunk was visible in multiple short-axis slices, we refer to the component closest to the right ventricle as the pulmonary root, and the distal-most component as the proximal pulmonary artery. The proximal pulmonary artery diameter was computed from the same imaging slice during right ventricular systole and diastole. An estimate of pulmonary artery strain was computed, but this estimate is subject to significant limitations (see **Limitations**).

Comparison of right atrial area and volume measurements

As a sensitivity analysis, we compared the consistency over time of two right atrial measurement methods (four-chamber area vs area-length method, described in **Supplementary Methods**) in 2,436 individuals with imaging data at two separate imaging visits. The second visit, on average, occurred shortly after the first (mean 2.25 years; standard deviation 0.12 years). The maximum area measurement was more tightly correlated over time ($r = 0.851$) than the maximum volume measurement ($r = 0.840$). Therefore, we used the right atrial area-based measurements in our primary analyses.

Comparison to previous studies investigating heart size and function

The estimates of right atrial area from the four-chamber view, as reported in **Supplementary Tables 1-2**, are similar to those previously reported[3], as are the proximal pulmonary artery diameters[4]. The estimates of right ventricular stroke volume are comparable to prior reports, and

both end diastolic and end systolic volumes fall in between what has been previously reported for steady-state free precession magnetic resonance imaging[5,6]. Consequently, our right ventricular ejection fraction estimates also fall between those of Foppa, *et al*, and Bai, *et al*.

Right heart structures are correlated with their left heart counterparts

Our analysis of the cross-correlation between cardiac phenotypes included both right- and left heart structures(**Supplementary Figure 3**). The volumetric measurements of the right and left ventricles were well correlated with one another (correlation between ventricular volumes was 0.86 at end-diastole and 0.74 at end-systole). In contrast, there was weaker correlation between right and left ventricular ejection fraction (correlation 0.44). This is consistent with drivers of contractility being only partially shared between the two ventricles, as well as multiplicative error due to the calculation of ejection fraction from two separately measured volumes. The ventricles nevertheless had well correlated stroke volumes (correlation 0.90), which is expected because stroke volume at steady-state is nearly equal for both ventricles in the absence of valvular regurgitation or shunt.

The proximal pulmonary artery diameter measured in end systole was modestly positively correlated with RVESV (correlation 0.48) and showed a weak inverse correlation with right ventricular ejection fraction (correlation -0.23), suggesting shared influences on the pulmonary artery diameter and right ventricular size and function. In addition, the pulmonary artery diameter and that of the ascending aorta—which share an embryological origin—were modestly correlated (correlation 0.43).

Pre-existing cardiovascular diseases associated with abnormal right heart measurements

First, we tested for association with PheCode-based disease definitions, which are derived from hospital diagnosis codes[7]. The right heart phenotypes were strongly correlated with atrial arrhythmias. The right atrial phenotypes were also associated with valvular diseases; the right ventricular phenotypes with obesity and heart failure; and the pulmonary artery phenotypes with obesity, blood pressure, and sleep disorders (**Figure 2**, **Supplementary Table 3**).

Next, we focused on three diseases (atrial fibrillation, congestive heart failure, and pulmonary hypertension, defined in **Supplementary Table 4**) that have clinically established chamber-specific links to the right heart[8–10]. We identified 1,098 individuals with a diagnosis of atrial fibrillation or flutter prior to undergoing MRI; 282 with congestive heart failure; and 21 with pulmonary hypertension. In a linear model, the right atrial fractional area change (RA FAC) was 1.1 standard deviations (SD) lower among those with a history of atrial fibrillation or flutter than those without (P=2.2E-309). The right ventricular ejection fraction (RVEF) was 0.51 SD lower among those with heart failure (P=6.6E-19). The proximal pulmonary artery diameter was 1.0 SD larger among those with pulmonary hypertension (P=5.1E-06). These findings confirmed expected correlations with prevalent cardiovascular diseases.

Finally, for two cardiovascular diseases—pulmonary hypertension and congestive heart failure—we modeled right ventricular volume over the course of the cardiac cycle for individuals with and without disease (**Figure 3**). In these models, pulmonary hypertension (present in 21 participants) was associated with elevated right ventricular volume throughout the cardiac cycle, which persisted after adjustment for left ventricular volume. The excess volume that was attributable to disease accounted for as much as 21% of the total RV end systolic volume (RVESV), yielding a reduced RVEF (two-tailed P = 3.9E-04 against the null hypothesis of no effect). Congestive heart failure (present in 282 participants) was also associated with elevated RVESV in an analysis that was not adjusted for left ventricular volume (14% elevation; P = 5.2E-17; **Supplementary Figure 4**). However, after accounting for left ventricular volume, the presence of a heart failure diagnosis was associated with relatively spared right ventricular volume (9.6% reduction at end-systole; P = 6.9E-09). As a negative control, 3,949 participants with cataract—a disease of the lens of the eye that is not expected to be linked to right ventricular size—demonstrated no significant difference in right ventricular volume compared to cataract-free individuals.

GWAS quality control

Among the right heart traits, the phenotype with the greatest lambda genomic control (GC) was 1.15 from the RVEDV GWAS; *ldsc* revealed an intercept of 1.02, consistent with polygenicity rather than population stratification (**Supplementary Table 18**)[11]. Seven lead SNPs had Hardy-Weinberg equilibrium (HWE) P < 1E-06; re-analysis of those SNPs in a strictly European subset of samples resolved the HWE violations and yielded similar effect estimates (**Supplementary Table 19**).

Replication of pulmonary artery diameter loci in FHS

We found good concordance between the pulmonary artery (in systole) GWAS results and the effect estimates produced from genetic analysis of participants from the Framingham Heart Study (FHS) who had genetic data and pulmonary artery measurements available[12,13]. 28 of the lead SNPs for pulmonary artery diameter were identified in FHS. Of these, 25 had a concordant effect direction with the UK Biobank (binomial test two-tailed P = 2.7E-05; **Supplementary Table 11**). At stringent P value thresholds (UK Biobank P < 5E-08 or stronger), there was strong correlation between UK Biobank and FHS effect size estimates (r = 0.71 to 0.81; **Supplementary Figure 16**).

TWAS highlights role of WNT signaling in pulmonary root diameter

Across all phenotypes, the strongest GWAS association was between the pulmonary root diameter and rs17608766 (P = 3.1E-48), near *GOSR2*. In a transcriptome-wide association study (TWAS) based on gene expression data from the aorta from GTEx v7[14], at that locus we observed an association between pulmonary root diameter and *WNT9B* (all results with TWAS P < 0.05 in **Supplementary Table 20**). Interestingly, *WNT9B* is expressed in the endocardium overlying the heart valves during development, and loss of *WNT9B* leads to defective valve

formation[15]. In addition to this locus's associations with aortic valve area noted above[16], it was also recently shown to be linked with the mitral valve annular diameter[17].

The strongest TWAS association for the proximal pulmonary artery diameter was with *PDGFD*, which is also the nearest gene to the lead SNP rs2128739. *PDGFD* loss-of-function variants were recently implicated in pulmonary hypertension in a sequencing-based case-control study[18]. The pulmonary artery and pulmonary root TWAS results are depicted in **Supplementary Figure 18**.

We also conducted chamber-specific cell type enrichment analyses, using gene expression at the GWAS loci to identify relevant cell types associated with variation in each chamber. We performed stratified linkage disequilibrium (LD) score regression analysis that integrated single nucleus RNA-sequencing data from Tucker *et al*[19]. The strongest enrichment was seen between RVEF and right ventricular cardiomyocytes, while the strongest enrichment for the right atrial phenotypes was for vascular smooth muscle cell-like nuclei (**Supplementary Figure 19**). Future studies with larger sample sizes will be required to assess genotype-specific expression levels within each chamber.

GWAS loci enriched in uncommon and difficult to phenotype cardiac diseases

We sought to investigate the association between loci identified in this study and diseases that are not well represented, such as congenital heart diseases, or difficult to identify due to lack of specific diagnostic codes in the electronic health record, such as arrhythmogenic right ventricular cardiomyopathy. We performed proximity-based testing to assess enrichment of gene sets near the GWAS loci and we identified disease-related gene sets using the OpenTargets platform v21.04 (gene lists in **Supplementary Table 21**)[20]. We then asked whether more of our loci than expected by chance were found within 500kb of the genes from each gene set. Note that because the number of permutations generated by SNPSnap in the following tests was 10,000, the strongest possible association P value was 1.0E-04[21].

Interestingly, the right atrial loci were in proximity to eight atrial septal defect-related genes (*DMPK*, *FOXP1*, *GATA4*, *MYH6*, *NKX2-5*, *NRG1*, *NSF*, *RBM45*) with one-tailed permutation P = 2.8E-03. The right ventricular GWAS loci were in proximity to 10 ARVC-related genes (*BAG3*, *DSP*, *JUP*, *MTO1*, *OBSCN*, *PLEC*, *PPP1R13L*, *RBM20*, *TMEM43*, *TTN*) with P = 1.0E-04. And the pulmonary artery loci were in proximity to nine conotruncal abnormality-linked genes (*BAZ1B*, *CHTOP*, *DVL2*, *DYNC2H1*, *GATA4*, *KAT6A*, *MECOM*, *NKX2-5*, *SMARCA4*) with P = 4.7E-03 (**Supplementary Figure 20**).

We also analyzed a previously described panel of 129 cardiomyopathy-linked genes to contrast RVESV loci with LVESV loci[22]. Eleven of these genes were within a 500kb radius of the RVESV loci; of these, seven (*ALPK3*, *BAG3*, *PLEKHM2*, *RBM20*, *SHOC2*, *TMEM43*, and *TTN*) were found near genome-wide significant LVESV loci; two (*GATA4* and *JUP*) were unique to the RVESV; and two (*MTO1* and *VCL*) were unique to the RVESV/LVESV ratio. The RVESV and

LVESV associations at the *GATA4* locus have been described above (**Supplementary Figure 13**). *JUP*, the gene that encodes plakoglobin, is a desmosomal protein that has also been associated with arrhythmogenic right ventricular cardiomyopathy and palmoplantar keratoderma, a syndrome known as Naxos disease (**Supplementary Figure 21**)[23–25]. Variants in *MTO1* are associated with hypertrophic cardiomyopathy[26], while variants in *VCL* are associated with pediatric-onset dilated cardiomyopathy[27].

Rare variant association analysis

Rare variant analyses were conducted in the 11,307 participants with exome data and right atrial measurements, 11,586 with right ventricular measurements, and up to 12,277 with pulmonary artery measurements. After accounting for multiple testing, no gene-phenotype association in the loss-of-function (LoF) collapsing burden test achieved a Bonferroni-corrected significance of P < 1.9E-06 (derived from 0.05/[26793 gene-phenotype pairs with >= 10 LoF variant carriers]). The strongest association was between LoF variants in *AAGAB* and pulmonary artery diameter (P = 2.6E-06); the full list of association results is provided in **Supplementary Table 22**.

RVEF polygenic score replication in MGB and BioBank Japan

We pursued external replication of the association between the RVEF polygenic score and dilated cardiomyopathy (DCM) in the Mass General Brigham BioBank (MGB)[28], where we found the RVEF polygenic score to be associated with DCM (1,414 cases and 21,972 controls; odds ratio [OR] 1.12 per SD decrease, P = 3.2E-05). After adjustment for a polygenic score produced from the LVESV indexed for body surface area (LVESVi) GWAS using PRScs-auto, this association remained significant (OR 1.11 per SD decrease, P = 8.0E-05)[29].

We also pursued external replication in BioBank Japan (BBJ), a Japanese-ancestry cohort[30,31]. In BBJ, the RVEF polygenic score was also inversely associated with DCM with a similar effect size to that seen in MGB (1,058 cases and 153,392 controls; OR 1.11 per SD decrease, P = 5.0E-04). After adjustment for the LVESVi score, this association attenuated to OR 1.05 per SD decrease (P = 0.08).

Pulmonary artery polygenic score replication in MGB, FHS, and BioBank Japan

In external validation, the PRScs-auto-derived polygenic score for the pulmonary artery diameter in systole remained significantly associated with pulmonary hypertension in MGB (866 cases and 23,230 controls; OR 1.11 per SD; P = 3.1E-03). However, this association did not replicate in BBJ (1,403 cases and 169,427 controls; OR 0.99 per SD; P = 0.77).

We also assessed the association between the pulmonary artery polygenic score and the quantitative measurement of the pulmonary artery diameter in an external cohort, the Framingham Heart Study (FHS)[32]. In 3,093 FHS participants with pulmonary artery diameter measurements and genetic data, a one SD increase in the polygenic score was associated with

a 0.17 SD increase in pulmonary artery diameter (P = 2.1E-21). The R^2 of the model attributable to the polygenic score was 0.026. Based on our heritability estimate of 0.397, these results are consistent with the polygenic score accounting for 6.5% of the heritability of pulmonary artery diameter in this external cohort.

Technical limitations related to MRI acquisition and deep learning

The individuals who underwent MRI in the UK Biobank tend to be healthier than the remainder of the UK Biobank population, which itself is healthier than the general population. Because of limited follow-up time after MRI with few events to date, an incident disease analysis accounting for measured right heart phenotypes was not conducted in the subgroup of participants with MRI data in the UK Biobank. Dedicated right ventricular outflow tract views were not obtained as part of the UK Biobank imaging protocol, and therefore we have derived pulmonary artery measurements from basal short axis images. The right ventricular infundibulum has not been measured separately, but rather has been counted toward the right ventricular blood pool, consistent with previous analyses of the UK Biobank[33]. The short axis cardiovascular magnetic resonance images have a coarse 10mm spacing, which leads to partial volume imaging that can be particularly difficult to visualize at the apex of the right ventricle. This leads to under- or over-estimation by human annotators and deep learning models. We have attempted to correct for this by incorporating the higher resolution four-chamber long axis data during the surface reconstruction process of the right ventricle. Participants' cardiac rhythm at the time of MRI (particularly normal sinus rhythm versus atrial fibrillation) was not adjudicated.

All measurements were derived from deep learning models of short axis or four-chamber long axis views from cardiovascular magnetic resonance imaging. The deep learning models have imprecision that would be reduced with larger training sets, such as those used by Bai, *et al*[34]. Like any deep learning model, these models can produce non physiologic measurements when presented with images that contain features not seen in the training data. An advantage of the semantic segmentation approach in this work is that outliers can be visually inspected and the model re-trained as needed. The deep learning models have not been tested outside of the specific devices and imaging protocols used by the UK Biobank and are unlikely to generalize to other data sets without additional fine-tuning. The right atrial measurements are two-dimensional estimates of a three-dimensional structure and therefore cannot capture complete information about atrial volume. Pulmonary artery pressure measurements were not available, and therefore pulmonary artery distensibility was not computed. Pulmonary artery strain accuracy is further limited due to the descent of the heart during ventricular systole, causing the pulmonary artery diameter in systole and diastole to be measured at different locations along the length of the pulmonary artery, which likely causes strain to be underestimated. In future work, it would be interesting to assess the value of taking measurements that account for the descent of the heart for pulmonary artery measurements, which may improve the precision of strain estimates.

Supplementary Methods

Cardiovascular magnetic resonance imaging protocols

At the time of this study, the UK Biobank had released images in over 45,000 participants of an imaging substudy that is ongoing[35,36]. Cardiovascular magnetic resonance imaging was performed with 1.5 Tesla scanners (Syngo MR D13 with MAGNETOM Aera scanners; Siemens Healthcare, Erlangen, Germany), and electrocardiographic gating for synchronization[36]. Several cardiac views were obtained. For this study, two views (the long axis four-chamber view and the short axis view) were used. In both of these views, balanced steady-state free precession cines, consisting of a series of 50 images throughout the cardiac cycle for each view, were acquired for each participant[36]. For the four-chamber images, only one imaging plane was available for each participant, with an imaging plane thickness of 6mm and an average pixel width and height of 1.83mm. For the short axis view, several imaging planes were acquired. Starting at the base of the heart, 8mm-thick imaging planes were acquired with approximately 2mm gaps between each plane, forming a stack perpendicular to the longitudinal axis of the left ventricle to capture the ventricular volume. For the short axis images, the average pixel width and height was 1.86mm.

Deep learning model development

We had initially developed a deep learning model for annotating the right and left ventricular blood pools from short axis images based on 250 randomly chosen images, using similar hyperparameters to those described in the **Online Methods**. When visualizing the output from that model, we noted a recurring pattern of errors: the left and right atrium and proximal pulmonary artery (which were unlabeled at the time) were occasionally mis-labeled as being a part of the right or left ventricular blood pool. This motivated us to annotate those structures in the training data. Subsequently, we observed that the accuracy of the right ventricular blood pool segmentation was higher after training with 500 images than with 250. Therefore, we increased the number of segmented training images by approximately half again (to just over 750, of which 714 were used for training), at which point we did not observe a substantial change in model accuracy. Retrospectively, we re-trained the same segmentation architecture with a range of training data sample sizes (from 50 to 714 training samples) using 5-fold cross-validation in order to demonstrate the change in Dice score as the number of training samples increased (**Supplementary Figure 22**).

Deep learning model output quality control

Accuracy of the four-chamber long axis and short axis deep learning models was assessed with additional manually annotated images that were not used for model training or validation, with each annotation category (such as right ventricular blood pool) evaluated based on the Sørensen-Dice coefficient[37,38], which scales from 0 (no agreement between manual and automated annotations) to 1 (perfect agreement). Images with no pixels assigned to a feature by either the truth labels or the deep learning model output were assigned to have a Dice coefficient of 1 unless otherwise specified.

Right atrial measurements from the four-chamber long axis view

Three long-axis views were obtained in the UK Biobank (two-chamber, three-chamber, and four-chamber). Of these, only the four-chamber view reliably captures the right atrium. We therefore treated the right atrium as a planar surface, counting the pixels that were labeled by the four chamber semantic segmentation model as right atrium, and multiplying that number by the height and width of each pixel to obtain a right atrial area (with units of cm^2). For each individual, we obtained the maximum atrial area, the minimum atrial area, and the fractional area change (maximum area minus minimum area, divided by maximum area).

As a sensitivity analysis, we computed right atrial volumes using the area-length formula from the four-chamber data. First, we converted the MRI slices into 1-voxel thick structured grids co-rotated into the patient reference system. Then, we approximated the basal plane (i.e., at the level of the tricuspid valve) by fitting a line through the centers of the voxels located along the boundary separating the segmented RA and RV. We then took the line segment orthogonal to this boundary, on the plane of the four-chamber view, yielding the length (L). The area-length estimate for right atrial volume was then calculated as $\left(\frac{8}{3\pi}\right) \cdot \frac{A_{4Ch}^{2}}{L}$, where A_{4Ch} is the area of the right atrium in the four-chamber view[5]. An analysis comparing the consistency of the right atrial area and volume estimates was conducted in individuals who had undergone imaging at two different visits (UK Biobank first and second imaging visits).

Pulmonary artery measurements from the short axis view

For many individuals in the UK Biobank, the pulmonary root and proximal pulmonary artery can be visualized in the basal-most short axis imaging planes. We refer to the apical-most segment that is visible just basal to the right ventricular outflow tract as the “pulmonary root.” We refer to the distal-most segment of the main pulmonary artery (visible in the basal-most short axis imaging plane) as the “proximal pulmonary artery.” When the pulmonary structures were visible in only one short axis plane, we assigned the measurement of this structure to be the pulmonary root, and assigned a missing value to the maximum and minimum pulmonary artery diameters for that individual. For participants in whom the proximal pulmonary artery was visible, we extracted measurements at two times in the cardiac cycle from the same short axis slice: once during right ventricular systole, and once during right ventricular diastole, designed to place physiological constraints on the timing of the expected maximum and minimum pulmonary diameter, respectively, throughout the cardiac cycle.

After visualizing deep learning model output, we developed heuristics for quality control. The pulmonary root and proximal pulmonary artery were treated as ellipses. We computed major and minor axes using classical image moment algorithms[1,2]. For both the proximal pulmonary artery and the pulmonary root, the length of the minor elliptical axis (i.e., the diameter) was computed. We excluded any measurements where the artery was divided into more than one connected component[39]. For the proximal pulmonary artery, we permitted elliptical eccentricity values of up to 0.85 (where eccentricity is $\sqrt{1-\frac{b^2}{a^2}}$, with *a* being the elliptical major axis and *b*

being the elliptical minor axis). We permitted a liberal eccentricity cutoff for the proximal pulmonary artery because a common cause of high eccentricity was out-of-plane curvature of the proximal pulmonary artery, which erroneously elongates the major elliptical axis but does not significantly affect the minor elliptical axis (which we treated as the diameter). In contrast, for the pulmonary artery root, we required an eccentricity below 0.77. We used this more stringent cutoff at the root because we observed that a common cause of high eccentricity in these images was partial imaging of the right ventricle, which can spuriously foreshorten the minor elliptical axis of the pulmonary root. In addition, we excluded images where the cross-sectional area of the pulmonary artery was less than 2 cm^2.

We calculated a one-dimensional pulmonary artery strain estimate based on the systolic and diastolic pulmonary artery diameter, where strain can be represented as $\frac{(systole - diastole)}{diastole}$. Because of the descent of the heart during ventricular systole, strain was not always positive; we excluded negative strain measurements (discussed more in the **Limitations** section).

Right ventricular annotation and Poisson surface reconstruction integrating long- and short-axis data

The right ventricle was visible in two separate views (short axis and four-chamber long axis), permitting a reconstruction of its volume through the incorporation of these orthogonal data. Stacked together, images from the short axis view provided a complete 3-dimensional representation of the right ventricle; however, this stack had a coarse 10mm resolution along the length of the right ventricle from base to apex. In contrast, the four-chamber long axis view had approximately 2mm resolution along the same axis. To take advantage of the strengths of both sources of data, we reconstructed the surface of the right ventricle using a Poisson surface reconstruction technique described in detail below. This enabled the computation of right ventricular end diastolic volume, end systolic volume, stroke volume, and ejection fraction.

To produce consistent estimates of the RV volumes throughout the cardiac cycle, we integrated information from the long- and short-axis segmentations by reconstructing 3-dimensional surfaces enclosing the RV cavity. We first used image metadata from the standard *Image Position (Patient) [0020,0032]* and *Image Orientation (Patient) [0020,0037]* DICOM tags to co-rotate the 4-chamber and short-axis slices into the same reference system. Then, we implemented a custom reconstruction routine based on the Poisson algorithm to generate surfaces that fitted through the boundaries of the RV segmentations[40]. As the Poisson algorithm requires local curvature as an input, we specified for the surface normal directions to lie onto the plane of the MRI slices and to be locally oriented towards either the pericardium (at the free wall) or the left ventricle (at the interventricular septum). The reconstructed RVs were then post-processed to correct for eventual artifacts in the basal short-axis slices, where the segmentation model may occasionally mistake the right atrium for part of the RV. Leveraging the fine resolution of the long-axis CMR in the apex-to-base direction, we discarded the portions of the reconstructed RVs that overextended above the plane separating the long-axis segmentations of the right atrium and of the RV (i.e., approximately co-aligned with the tricuspid valve plane). Finally, the RV volumes were estimated from the reconstructed surfaces using a discrete

version of the divergence theorem, as implemented in the open-source VTK library (Kitware Inc.).

Left heart phenotype measurements

To gain a better understanding of the distinction between genetic contributions to right and left heart structures, we also conducted analyses of the aortic diameter (paired with the pulmonary artery) and the left ventricular blood pool (paired with the right ventricular structures derived above). The aortic diameter derivation was previously described[2]; in brief, we trained a deep learning model to perform semantic segmentation of the ascending aorta in the same UK Biobank participants using the aortic distensibility view, and applied that model to all participants with available images. Left ventricular measurements were extracted from the same deep learning model output that was used to measure the right ventricular blood pool from the short axis images. The pixels were multiplied by their height, width, and depth to estimate a volume for each short axis image, and these per-image volumes were summed across all short axis images to produce left ventricular volumes for each participant. This enabled the computation of left ventricular end diastolic volume (LVEDV), end systolic volume (LVESV), stroke volume (LVSV), and ejection fraction (LVEF).

Phenotypic characterization of right heart structure and function

Using R version 3.6, we evaluated the mean and standard deviation of the right heart measurements, described them in age- and sex-stratified tables, and created sex-stratified kernel density plots with *ggplot2*[41]. We computed the Pearson correlation between all right heart phenotypes and available left heart phenotypes that were previously described[2,22].

We tested for association between the right heart phenotypes and PheCode-based disease labels derived from ICD-10 codes and OPCS-4 codes[7]. The model was formulated as a linear model with the right heart phenotype as the outcome variable, with independent variables including the presence or absence of disease as a binary variable, and clinical covariates that included MRI serial number, sex, the first five principal components of ancestry, age at enrollment, the cubic natural spline of age at the time of MRI, and the genotyping array. This test was repeated for each disease and for each right heart phenotype. Splines were not placed on age at enrollment because of its collinearity with age at the time of MRI.

We used three custom disease definitions to focus on chamber-specific disease relationships (atrial fibrillation with RA FAC; heart failure with RVESV; and pulmonary hypertension with the proximal pulmonary artery diameter; defined in **Supplementary Table 4**). Association between each prevalent disease (as a binary independent variable) and the right heart phenotypes (as the dependent variable) was performed using a linear model that also accounted for the MRI serial number, sex, the first five principal components of ancestry, age at enrollment, the cubic natural spline of age at the time of MRI, and the genotyping array. As above, splines were not placed on age at enrollment because of its collinearity with age at the time of MRI.

We also modeled the association between three diseases (pulmonary hypertension, heart failure, and cataract) and right ventricular volume throughout the cardiac cycle. The magnetic resonance images were acquired as a series of 50 images throughout a cardiac cycle, and so our Poisson surface reconstruction yielded right ventricular volume for each of these timepoints (one-fiftieth of a cardiac cycle). At each of these timepoints, we used a linear model to test the association between the right ventricular volume (independent variable) and the presence or absence of each of the three diseases, as well as covariates that included weight, height, age at enrollment, the cubic natural spline of age at the time of MRI, sex, genotyping array, and the first five principal components of ancestry. We repeated this with and without adjustment for left ventricular volume. In the results, we report the P value for the linear model regression coefficient for the disease. To model the estimated volume for individuals with or without disease, we compute the output of the linear model for a 55-year-old woman who enrolled 5 years previously in the UK Biobank, 162 centimeters tall and weighing 75.6 kilograms. We then toggle the presence or absence of disease in the model to obtain volumes with or without disease, fixing other covariates.

Transcriptome-wide association study

We performed TWAS to identify correlated genes based on imputed cis-regulated gene expression[42–44]. We used FUSION (version: http://gusevlab.org/projects/fusion/ version sha1@0ab190e) with eQTL data from GTEx v7. Precomputed transcript expression reference weights for the aorta (used for the pulmonary artery traits), left ventricle (used for the right ventricular traits), and right atrial appendage (used for the right atrial traits) were obtained from the FUSION authors' URL listed above[14,43]. FUSION was then run with its default settings.

OpenTargets gene set enrichment at GWAS loci

Using the OpenTargets platform version 21.04, we obtained gene sets corresponding to arrhythmias, channelopathies, myocardial diseases, and congenital anomalies by fetching all genes with an overall association score of 0.05 or greater (**Supplementary Table 21**)[20]. Using SNPsnap, we generated 10,000 sets of SNPs that matched our lead SNPs based on parameters including minor allele frequency, SNPs in linkage disequilibrium, distance from the nearest gene, and gene density. We counted the number of loci with lead SNPs from our study that fell within 500kb of one or more genes from each OpenTargets gene set. We then repeated the same procedure for each of the 10,000 synthetic SNPsnap lead SNP lists, to set a neutral expectation for the number of loci near an OpenTargets gene based on chance. This allowed us to compute one-tailed permutation P values for each group of disease genes (with the most extreme possible P value based on 10,000 randomly chosen sets of SNPs being $1 \cdot 10^{-4}$). This procedure was performed with the *mendel* software, available at https://github.com/carbocation/genomisc[2].

Exome sequencing and rare variant association analysis

We conducted an exome sequencing analysis in the first 50,000 exomes released by the UK Biobank. Exome sequencing was performed by Regeneron and reprocessed centrally by the UK

Biobank following the Functional Equivalent pipeline[45]. Exomes were captured with the IDT xGen Exome Research Panel v1.0, and sequencing was performed with 75-base paired-end reads on the Illumina NovaSeq 6000 platform using S2 flowcells. Alignment to GRCh38 was performed centrally with BWA-mem[46]. Variant calling was performed centrally with GATK 3.0[47]. Variants were hard-filtered if the inbreeding coefficient was < -0.03, or if none of the following were true: read depth was greater than or equal to 10; genotype quality was greater than or equal to 20; or allele balance was greater than or equal to 0.2. Variants were annotated with the Ensembl Variant Effect Predictor version 95 using the --pick-allele flag[48]. LOFTEE 1.0 was used to identify high-confidence loss of function variants: stop-gain, splice-site disrupting, and frameshift variants[49]. In total, 49,997 exomes were available, of which a subset overlapped with a subset of the participants who had undergone magnetic resonance imaging. We restricted our analysis to the European genetic inlier subset of participants (described in **Online Methods>Polygenic score analysis**). We conducted collapsing burden tests with loss-of-function variants. Variants with MAF >= 0.001 were excluded. We excluded genes with fewer than 10 loss-of-function variants passing the above criteria. Based on its importance in cardiovascular disease, we additionally evaluated *TTN* when only accounting for variants found within exons that are expressed in more than 85% of *TTN* transcripts in cardiac tissue ("TTN_HIGHPSI")[50]. The collapsing burden test models were adjusted for weight (kg), height (cm), body mass index (kg/m^2), the MRI serial number, age at enrollment, the cubic natural spline of age at the time of MRI, sex, the genotyping array, and the first five principal components of ancestry.

Analysis of polygenic scores in BBJ, MGB, and FHS

We pursued replication of the RV and PA polygenic scores in three external biobanks: BioBank Japan (BBJ), the Mass General Brigham Biobank (MGB), and the Framingham Heart Study (FHS).

In BBJ, genetic data were available for 1099166 of the 1117425 score weights (98.4%). The analyses were modeled with logistic regression, modeling the presence or absence of disease using the scaled polygenic score, plus age, sex, and the first five principal components of ancestry as covariates. For the dilated cardiomyopathy analysis, this procedure was also repeated using a model that additionally accounted for the LVESVi polygenic score.

In MGB, genetic data were available for all score weights. The analyses were modeled as logistic regression, modeling the presence of absence of disease using the scaled polygenic score, plus sex, cohort, and the first five principal components of ancestry as covariates. For the dilated cardiomyopathy analysis, this procedure was also repeated using a model that additionally accounted for the LVESVi polygenic score.

In FHS, genetic data were available for 1099807 of the 1117425 score weights (98.4%). The analysis was modeled as linear regression, modeling the pulmonary artery diameter measurements using the scaled polygenic score, plus age, sex, and the first five principal components of ancestry as covariates. This procedure was repeated without the polygenic

score to allow for the determination of the additional gain in model R^2 attributable to the polygenic score.

Supplementary References

1. Horn, B. *Robot vision*. (MIT Press ; McGraw-Hill, 1986).
2. Pirruccello, J. P. *et al.* Deep learning enables genetic analysis of the human thoracic aorta. *Nat Genet* (2021) doi:10.1038/s41588-021-00962-4.
3. Maceira, A. M., Cosín-Sales, J., Roughton, M., Prasad, S. K. & Pennell, D. J. Reference right atrial dimensions and volume estimation by steady state free precession cardiovascular magnetic resonance. *J Cardiovasc Magn Reson* **15**, 29 (2013).
4. Burman, E. D., Keegan, J. & Kilner, P. J. Pulmonary artery diameters, cross sectional areas and area changes measured by cine cardiovascular magnetic resonance in healthy volunteers. *Journal of Cardiovascular Magnetic Resonance* **18**, 12 (2016).
5. Bai, W. *et al.* A population-based phenome-wide association study of cardiac and aortic structure and function. *Nature Medicine* 1–9 (2020) doi:10.1038/s41591-020-1009-y.
6. Foppa, M. *et al.* Right Ventricular Volumes and Systolic Function by Cardiac Magnetic Resonance and the Impact of Sex, Age, and Obesity in a Longitudinally Followed Cohort Free of Pulmonary and Cardiovascular Disease: The Framingham Heart Study. *Circ Cardiovasc Imaging* **9**, e003810 (2016).
7. Wu, P. *et al.* Mapping ICD-10 and ICD-10-CM Codes to Phecodes: Workflow Development and Initial Evaluation. *JMIR Med Inform* **7**, e14325 (2019).
8. Edwards, P. D., Bull, R. K. & Coulden, R. CT measurement of main pulmonary artery diameter. *BJR* **71**, 1018–1020 (1998).
9. Melenovsky, V., Hwang, S.-J., Lin, G., Redfield, M. M. & Borlaug, B. A. Right heart dysfunction in heart failure with preserved ejection fraction. *Eur Heart J* **35**, 3452–3462 (2014).
10. Sanfilippo, A. J. *et al.* Atrial enlargement as a consequence of atrial fibrillation. A prospective echocardiographic study. *Circulation* **82**, 792–797 (1990).

11. Bulik-Sullivan, B. K. *et al.* LD Score regression distinguishes confounding from polygenicity in genome-wide association studies. *Nature Genetics* **47**, 291–295 (2015).
12. Is, R. *et al.* Distribution, Determinants, and Normal Reference Values of Thoracic and Abdominal Aortic Diameters by Computed Tomography (From the Framingham Heart Study). *The American journal of cardiology* (2013) doi:10.1016/j.amjcard.2013.01.306.
13. Qazi, S. *et al.* Increased Aortic Diameters on Multidetector Computed Tomographic Scan Are Independent Predictors of Incident Adverse Cardiovascular Events: The Framingham Heart Study. *Circ Cardiovasc Imaging* **10**, (2017).
14. Lonsdale, J. *et al.* The Genotype-Tissue Expression (GTEx) project. *Nature Genetics* **45**, 580–585 (2013).
15. Goddard, L. M. *et al.* Hemodynamic forces sculpt developing heart valves through a KLF2-WNT9B paracrine signaling axis. *Dev Cell* **43**, 274-289.e5 (2017).
16. Córdova-Palomera, A. *et al.* Cardiac Imaging of Aortic Valve Area From 34 287 UK Biobank Participants Reveals Novel Genetic Associations and Shared Genetic Comorbidity With Multiple Disease Phenotypes. *Circulation: Genomic and Precision Medicine* **13**, e003014 (2020).
17. Yu, M. *et al.* Computational estimates of mitral annular diameter in systole and diastole cardiac cycle reveal novel genetic determinants of valve function and disease. *medRxiv* 2020.12.02.20242206 (2020) doi:10.1101/2020.12.02.20242206.
18. Zhu, N. *et al.* Rare variant analysis of 4,241 pulmonary arterial hypertension cases from an international consortium implicate FBLN2, PDGFD and rare de novo variants in PAH. *bioRxiv* 2020.05.29.124255 (2020) doi:10.1101/2020.05.29.124255.
19. Tucker Nathan R. *et al.* Transcriptional and Cellular Diversity of the Human Heart. *Circulation* **142**, 466–482 (2020).
20. Mountjoy, E. *et al.* Open Targets Genetics: An open approach to systematically prioritize causal variants and genes at all published GWAS trait-associated loci. *bioRxiv*

2020.09.16.299271 (2020) doi:10.1101/2020.09.16.299271.

21. Pers, T. H., Timshel, P. & Hirschhorn, J. N. SNPsnap: a Web-based tool for identification and annotation of matched SNPs. *Bioinformatics* **31**, 418–420 (2015).
22. Pirruccello, J. P. *et al.* Analysis of cardiac magnetic resonance imaging in 36,000 individuals yields genetic insights into dilated cardiomyopathy. *Nature Communications* **11**, 1–10 (2020).
23. McKoy, G. *et al.* Identification of a deletion in plakoglobin in arrhythmogenic right ventricular cardiomyopathy with palmoplantar keratoderma and woolly hair (Naxos disease). *The Lancet* **355**, 2119–2124 (2000).
24. Protonotarios, N. & Tsatsopoulou, A. Naxos disease: Cardiocutaneous syndrome due to cell adhesion defect. *Orphanet Journal of Rare Diseases* **1**, 4 (2006).
25. Protonotarios, N. *et al.* Cardiac abnormalities in familial palmoplantar keratosis. *Br Heart J* **56**, 321–326 (1986).
26. Ghezzi, D. *et al.* Mutations of the Mitochondrial-tRNA Modifier MTO1 Cause Hypertrophic Cardiomyopathy and Lactic Acidosis. *Am J Hum Genet* **90**, 1079–1087 (2012).
27. Hawley, M. H. *et al.* An assessment of the role of vinculin loss of function variants in inherited cardiomyopathy. *Human Mutation* **41**, 1577–1587 (2020).
28. Karlson, E. W., Boutin, N. T., Hoffnagle, A. G. & Allen, N. L. Building the Partners HealthCare Biobank at Partners Personalized Medicine: Informed Consent, Return of Research Results, Recruitment Lessons and Operational Considerations. *J Pers Med* **6**, (2016).
29. Ge, T., Chen, C.-Y., Ni, Y., Feng, Y.-C. A. & Smoller, J. W. Polygenic prediction via Bayesian regression and continuous shrinkage priors. *Nature Communications* **10**, 1776 (2019).
30. Nagai, A. *et al.* Overview of the BioBank Japan Project: Study design and profile. *J Epidemiol* **27**, S2–S8 (2017).

31. Sakaue, S. *et al.* Dimensionality reduction reveals fine-scale structure in the Japanese population with consequences for polygenic risk prediction. *Nat Commun* **11**, 1569 (2020).
32. Truong Quynh A. *et al.* Reference Values for Normal Pulmonary Artery Dimensions by Noncontrast Cardiac Computed Tomography. *Circulation: Cardiovascular Imaging* **5**, 147–154 (2012).
33. Petersen, S. E. *et al.* Reference ranges for cardiac structure and function using cardiovascular magnetic resonance (CMR) in Caucasians from the UK Biobank population cohort. *Journal of Cardiovascular Magnetic Resonance* **19**, 18 (2017).
34. Bai, W. *et al.* Automated cardiovascular magnetic resonance image analysis with fully convolutional networks. *Journal of cardiovascular magnetic resonance : official journal of the Society for Cardiovascular Magnetic Resonance* **20**, 65 (2018).
35. Petersen, S. E. *et al.* Imaging in population science: cardiovascular magnetic resonance in 100,000 participants of UK Biobank - rationale, challenges and approaches. *Journal of Cardiovascular Magnetic Resonance* **15**, 46 (2013).
36. Petersen, S. E. *et al.* UK Biobank's cardiovascular magnetic resonance protocol. *J Cardiovasc Magn Reson* **18**, (2016).
37. Dice, L. R. Measures of the Amount of Ecologic Association Between Species. *Ecology* **26**, 297–302 (1945).
38. Sørensen, T. J. *A method of establishing groups of equal amplitude in plant sociology based on similarity of species content and its application to analyses of the vegetation on Danish commons.* (I kommission hos E. Munksgaard, 1948).
39. Rosenfeld, A. & Pfaltz, J. L. Sequential Operations in Digital Picture Processing. *J. ACM* **13**, 471–494 (1966).
40. Kazhdan, M. & Hoppe, H. Screened poisson surface reconstruction. *ACM Trans. Graph.* **32**, 29:1-29:13 (2013).
41. Wickham, H. *ggplot2: Elegant Graphics for Data Analysis*. (Springer-Verlag, 2009).

doi:10.1007/978-0-387-98141-3.

42. Gamazon, E. R. *et al.* A gene-based association method for mapping traits using reference transcriptome data. *Nat. Genet.* **47**, 1091–1098 (2015).
43. Gusev, A. *et al.* Integrative approaches for large-scale transcriptome-wide association studies. *Nat Genet* **48**, 245–252 (2016).
44. Zhu, Z. *et al.* Integration of summary data from GWAS and eQTL studies predicts complex trait gene targets. *Nat. Genet.* **48**, 481–487 (2016).
45. Regier, A. A. *et al.* Functional equivalence of genome sequencing analysis pipelines enables harmonized variant calling across human genetics projects. *Nature Communications* **9**, 4038 (2018).
46. Li, H. Aligning sequence reads, clone sequences and assembly contigs with BWA-MEM. *arXiv:1303.3997 [q-bio]* (2013).
47. Van der Auwera, G. A. *et al.* From FastQ data to high confidence variant calls: the Genome Analysis Toolkit best practices pipeline. *Curr Protoc Bioinformatics* **43**, 11.10.1-33 (2013).
48. McLaren, W. *et al.* The Ensembl Variant Effect Predictor. *Genome Biology* **17**, 122 (2016).
49. Karczewski, K. J. *et al.* The mutational constraint spectrum quantified from variation in 141,456 humans. *Nature* **581**, 434–443 (2020).
50. Roberts, A. M. *et al.* Integrated allelic, transcriptional, and phenomic dissection of the cardiac effects of titin truncations in health and disease. *Sci Transl Med* **7**, 270ra6 (2015).

Supplementary Figures

Supplementary Figure 1: Sample flow diagram

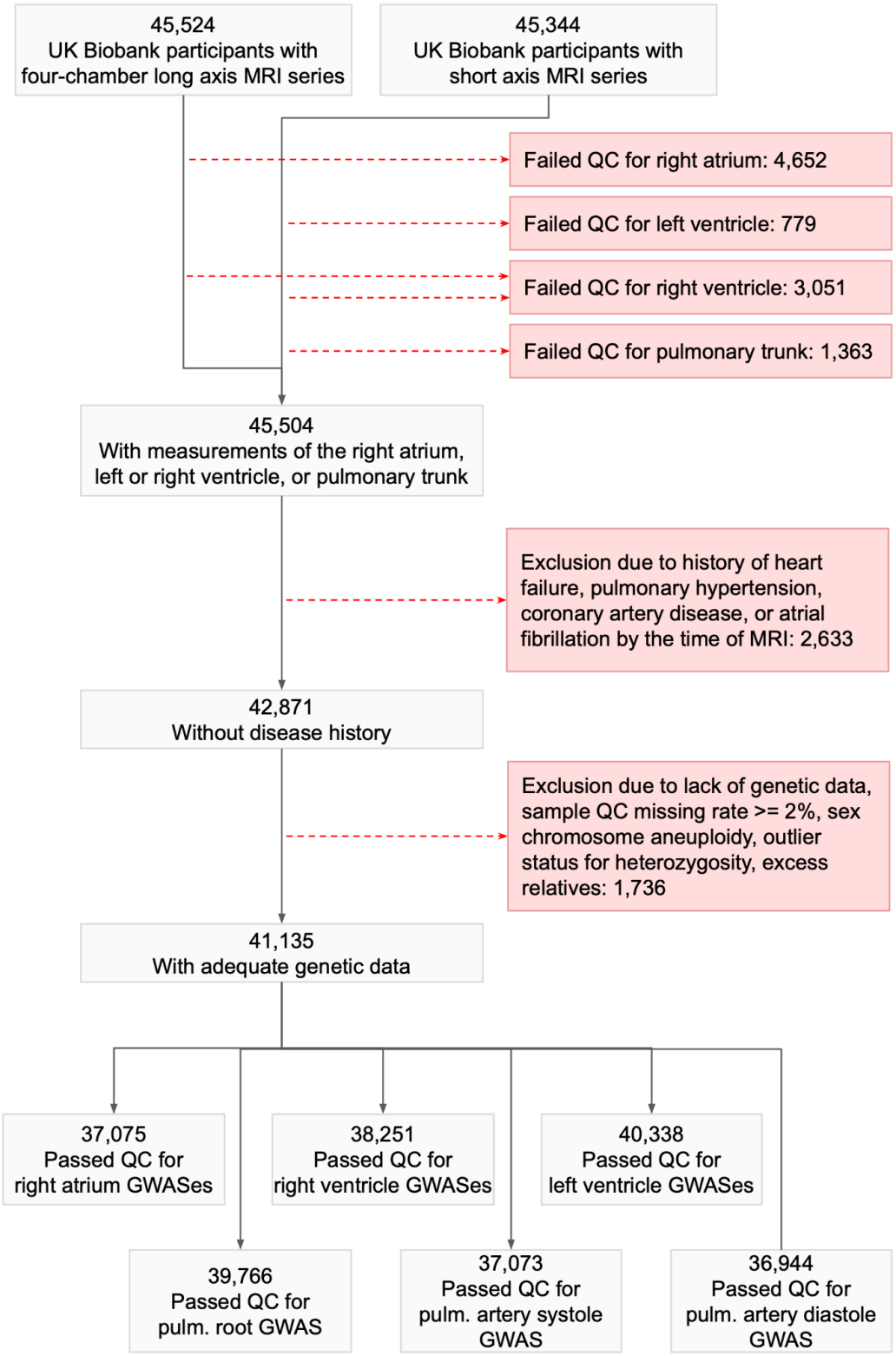

Supplementary Figure 2: Cardiac phenotype distributions

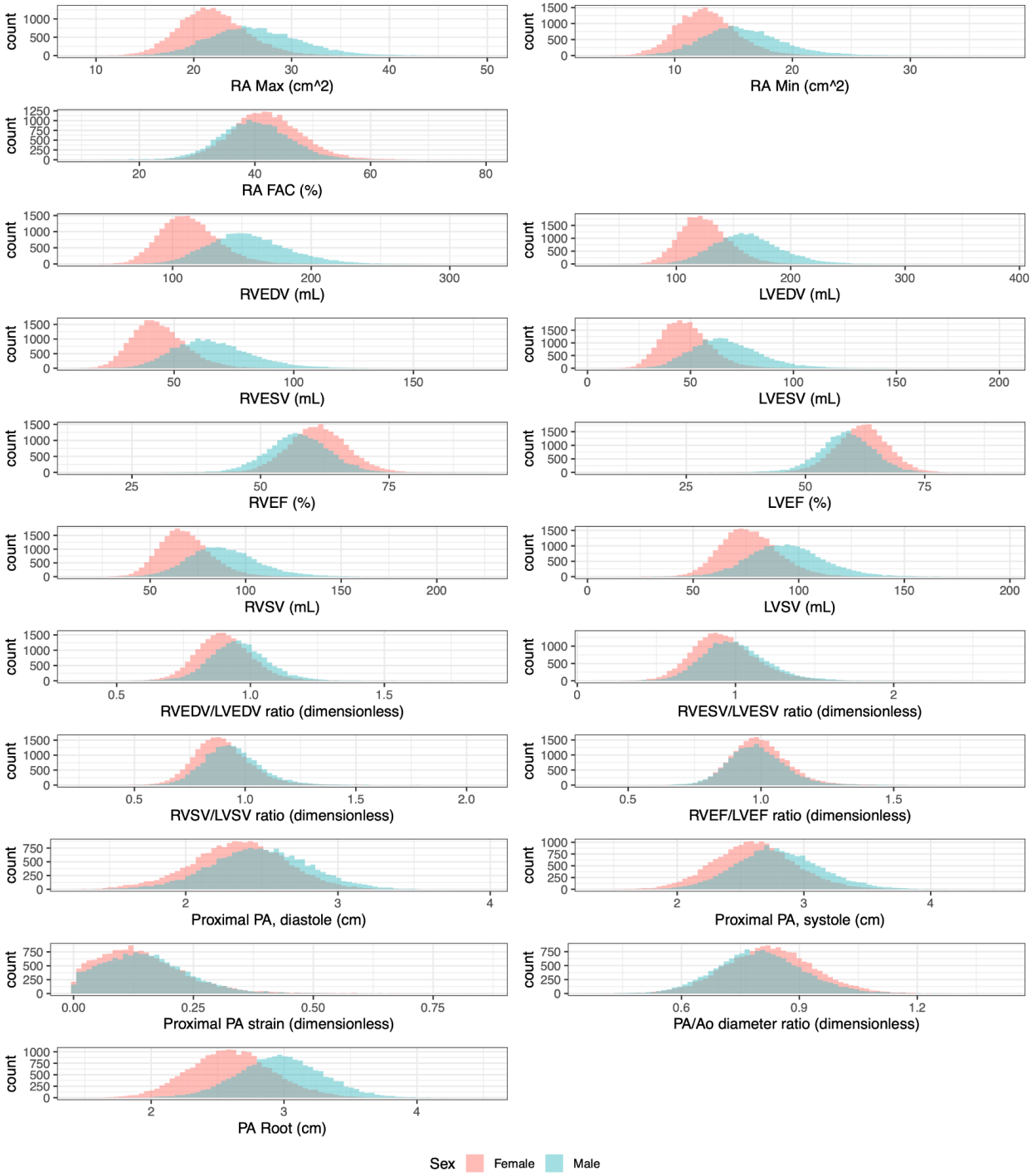

Histograms are shown for each trait in its natural units (**x axis**) with the number of individuals in each bucket on the **y axis**. Measurements for women are depicted in red and for men in turquoise.

Supplementary Figure 3: Correlation between cardiovascular imaging phenotypes

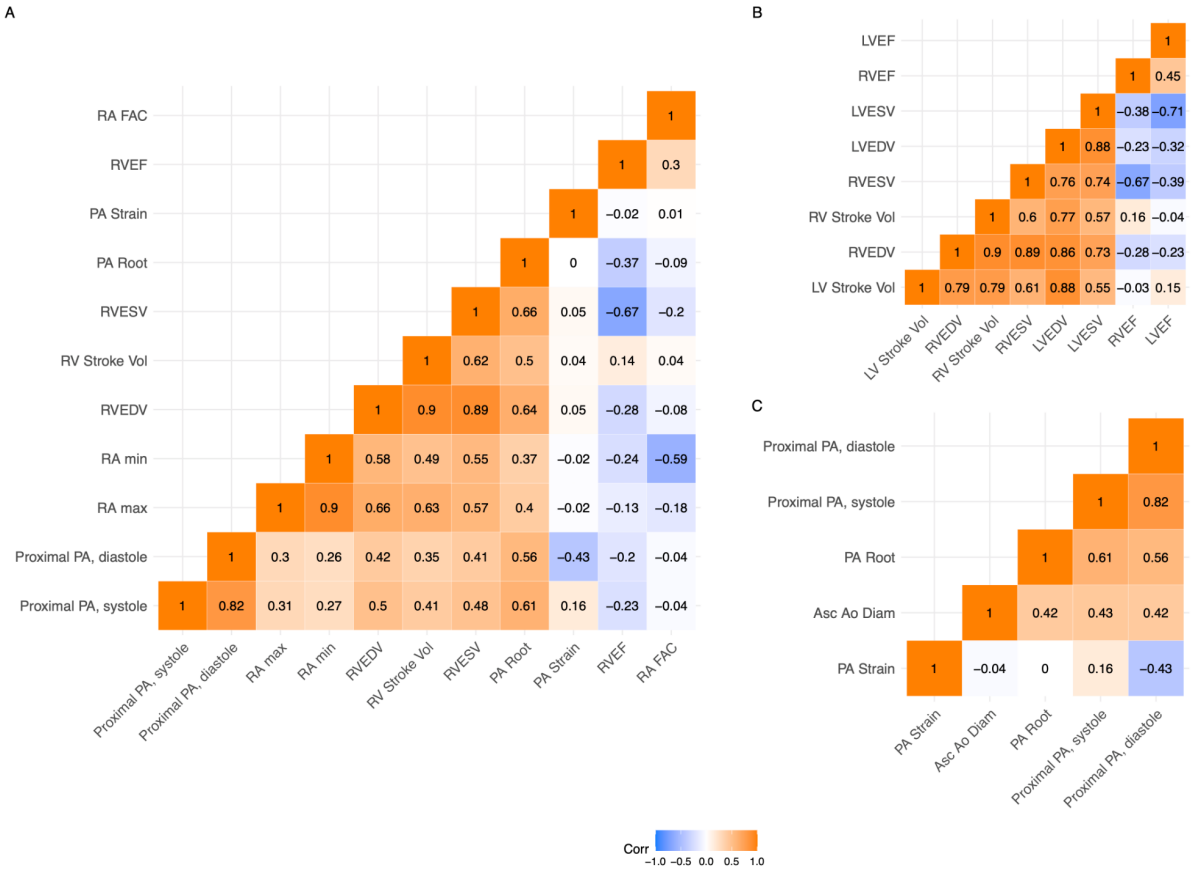

Plots showing the correlation between cardiovascular phenotypes. Phenotype order within each plot was arranged by hierarchical clustering. **Plot A**: All phenotypes. **Plot B**: Left and right ventricular phenotypes. **Plot C**: Pulmonary trunk and aortic phenotypes.

Supplementary Figure 4: Right ventricular volume curves without adjustment for left ventricular volumes

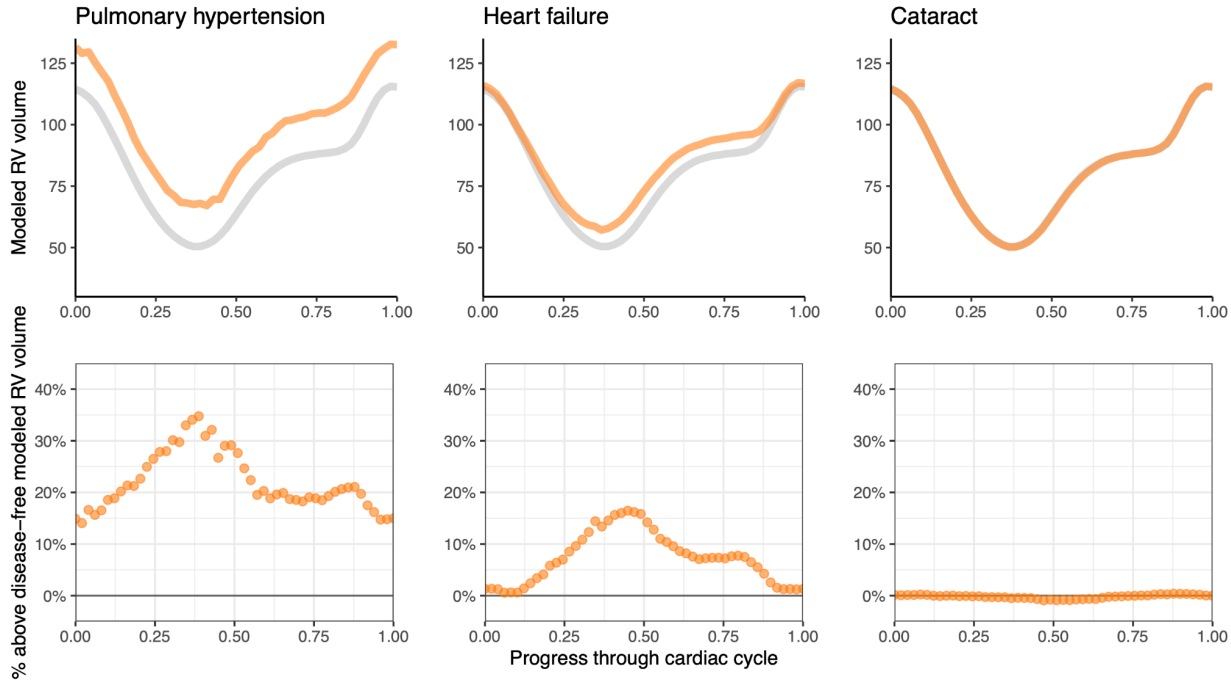

A variant of **Figure 3** without accounting for left ventricular volumes. **Top**: Disease diagnoses that occur prior to the date of MRI are linked with distinct changes in the volume of the right ventricle throughout the cardiac cycle. The x-axis represents fractions of a cardiac cycle (divided evenly into 50 components, starting at end-diastole). The y-axis represents volume in mL. Values are generated with a linear model for each time point accounting for clinical covariates; the gray line represents the population without disease, while the orange line represents the population with disease. In the UK Biobank, participants with pulmonary hypertension have elevated right ventricular volumes throughout the cardiac cycle. Those with heart failure predominantly have right ventricular volumes that are elevated but relatively spared when accounting for left ventricular volumes (see **Figure 3** for right ventricular volumes with adjustment for left ventricular volumes). Cataract is used as a control to demonstrate little association between a non-cardiovascular disease and the volume of the right ventricle. **Bottom**: At each time point, the right ventricular volume of individuals with disease is subtracted from the volume without disease and divided by the volume without disease. This represents the percentage above or below the disease-free right ventricular volume for those with disease.

Supplementary Figure 5: Genetic correlation between

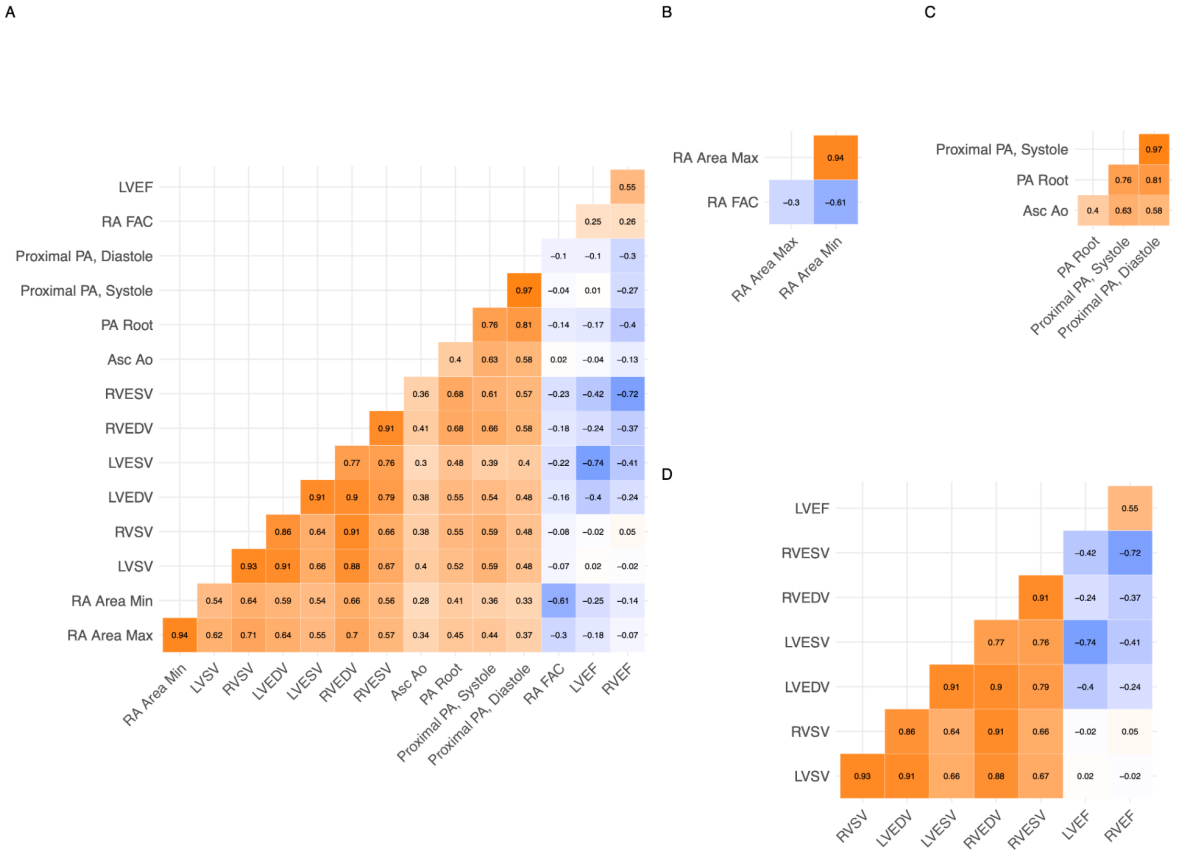

Grids of genetic correlations between cardiac phenotypes are shown. Phenotype order within each plot was arranged by hierarchical clustering. **Panel A**: All phenotypes (left and right ventricles, right atrium, pulmonary artery, and ascending aorta). **Panel B**: Right atrial phenotypes. **Panel C**: Aorta and pulmonary trunk. **Panel D**: Ventricular phenotypes. The value printed at the intersection of two different phenotypes represents the genetic correlation (rg) between the traits.

Supplementary Figure 6: GWAS quantile-quantile plots

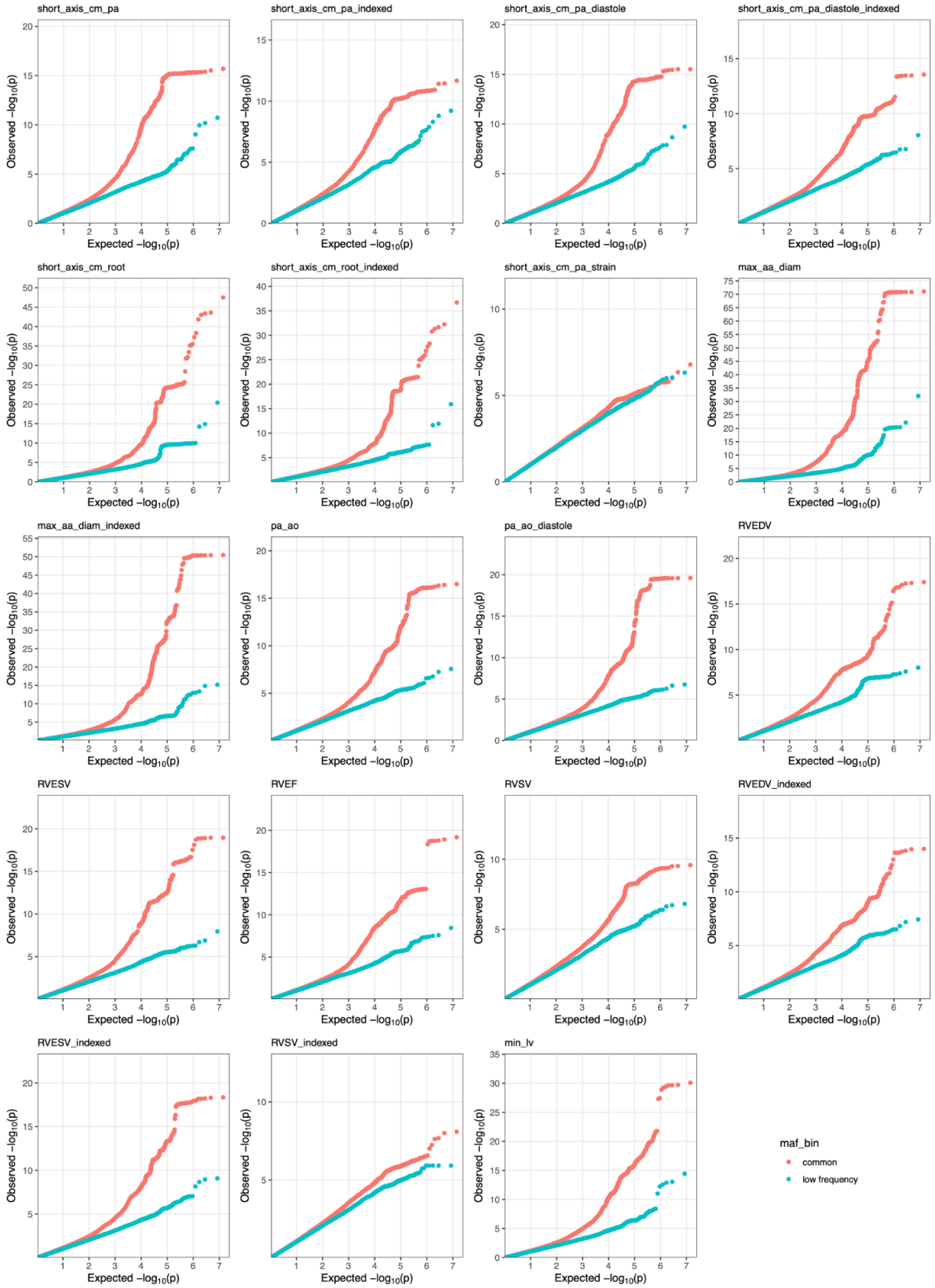

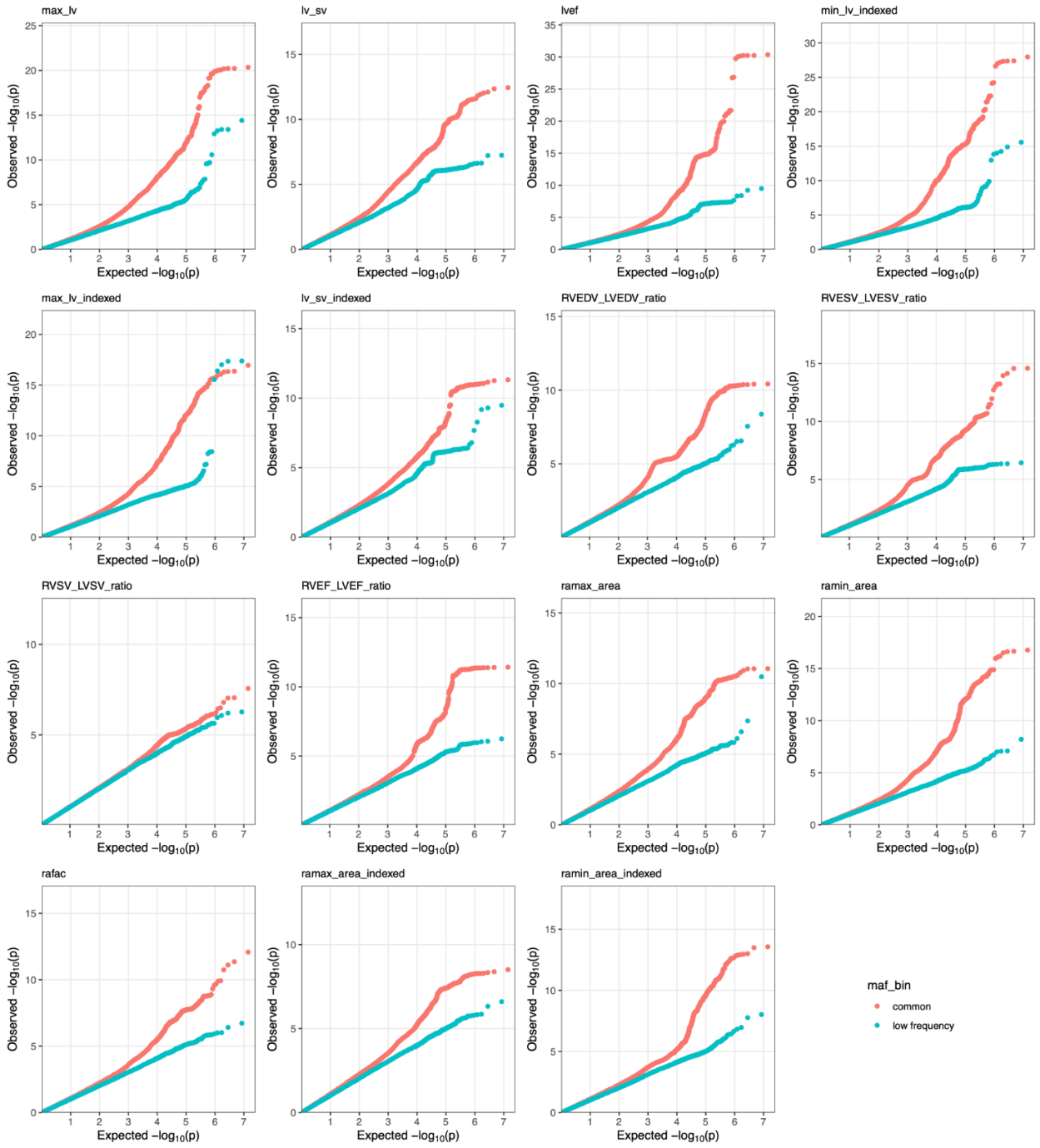

QQ-plots are displayed for each trait. SNPs are split between common (MAF >= 0.05) and low-frequency (MAF >= 0.005). Rare SNPs with MAF < 0.005 were excluded from our analysis.

Supplementary Figure 7: Right atrium Manhattan plots

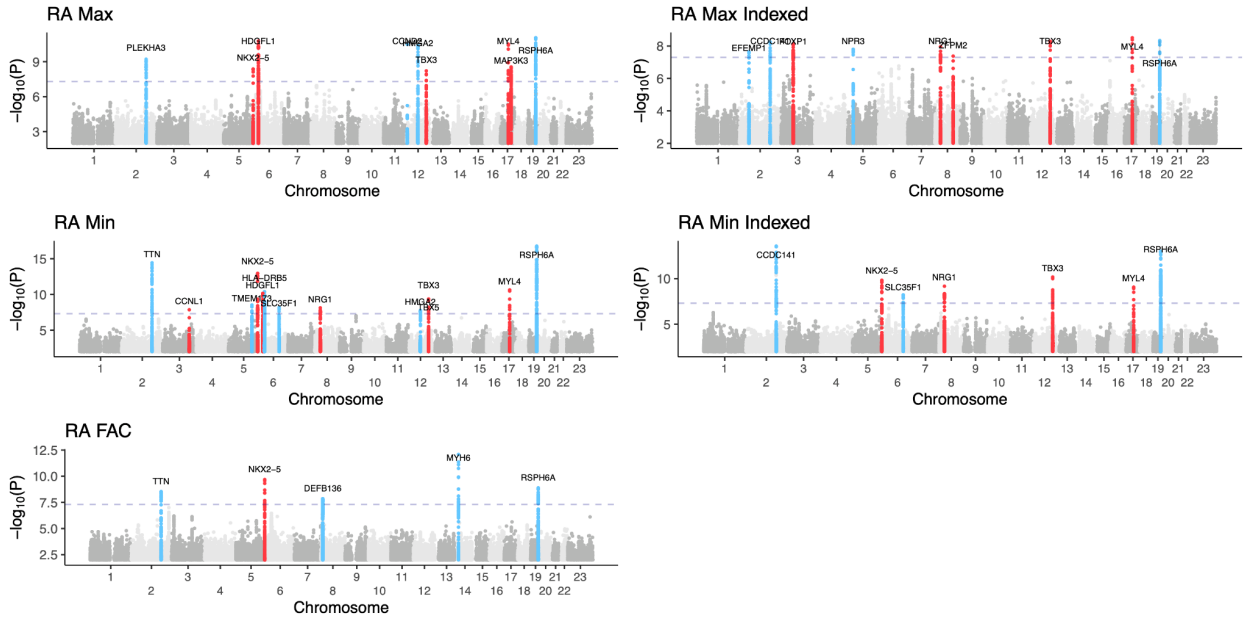

Manhattan plots are depicted for the right atrial traits. Where relevant, the left column contains the native trait, and the right column contains the body surface area indexed-trait. The **x axes** represent the chromosome and position. The X-chromosome is represented as “Chromosome 23.” The **y axes** represent the -$\log_{10}$(P), where P represents the BOLT-LMM association P value. Loci that contain SNPs with P < 5E-08 were labeled with the name of the nearest gene. These loci were colored blue if they were also associated with left heart phenotypes with P<5E-08, and otherwise were colored red.

Supplementary Figure 8: Right ventricle Manhattan plots

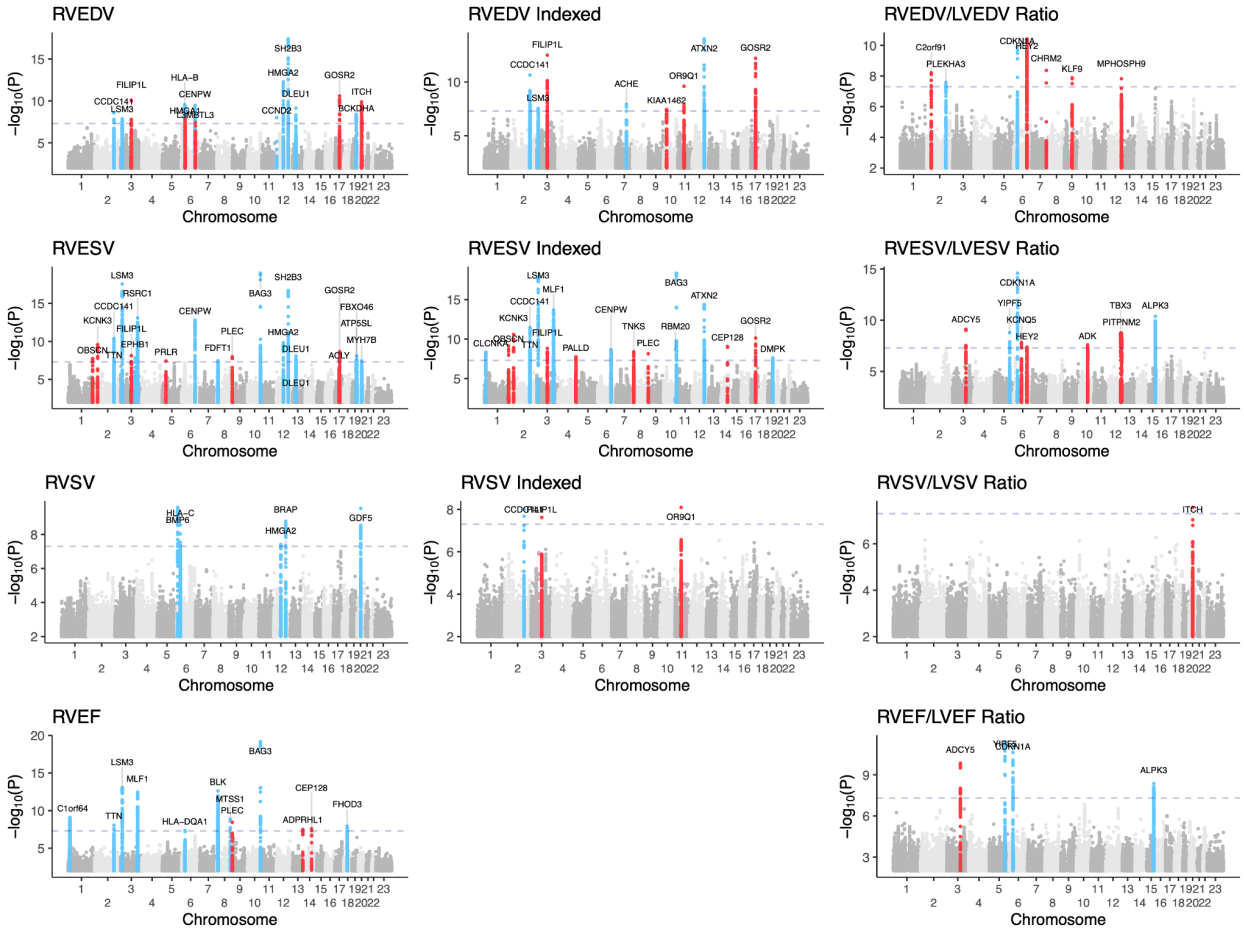

Manhattan plots are depicted for the ventricular traits. Where relevant, the leftmost column contains the native trait, the middle column contains the body surface area indexed-trait, and the rightmost column contains the trait indexed to its left heart-equivalent. The **x axes** represent the chromosome and position. The X-chromosome is represented as “Chromosome 23.” The **y axes** represent the -$\log_{10}$(P), where P represents the BOLT-LMM association P value. Loci that contain SNPs with P < 5E-08 were labeled with the name of the nearest gene. These loci were colored blue if they were also associated with left heart phenotypes with P<5E-08, and otherwise were colored red.

Supplementary Figure 9: Pulmonary artery Manhattan plots

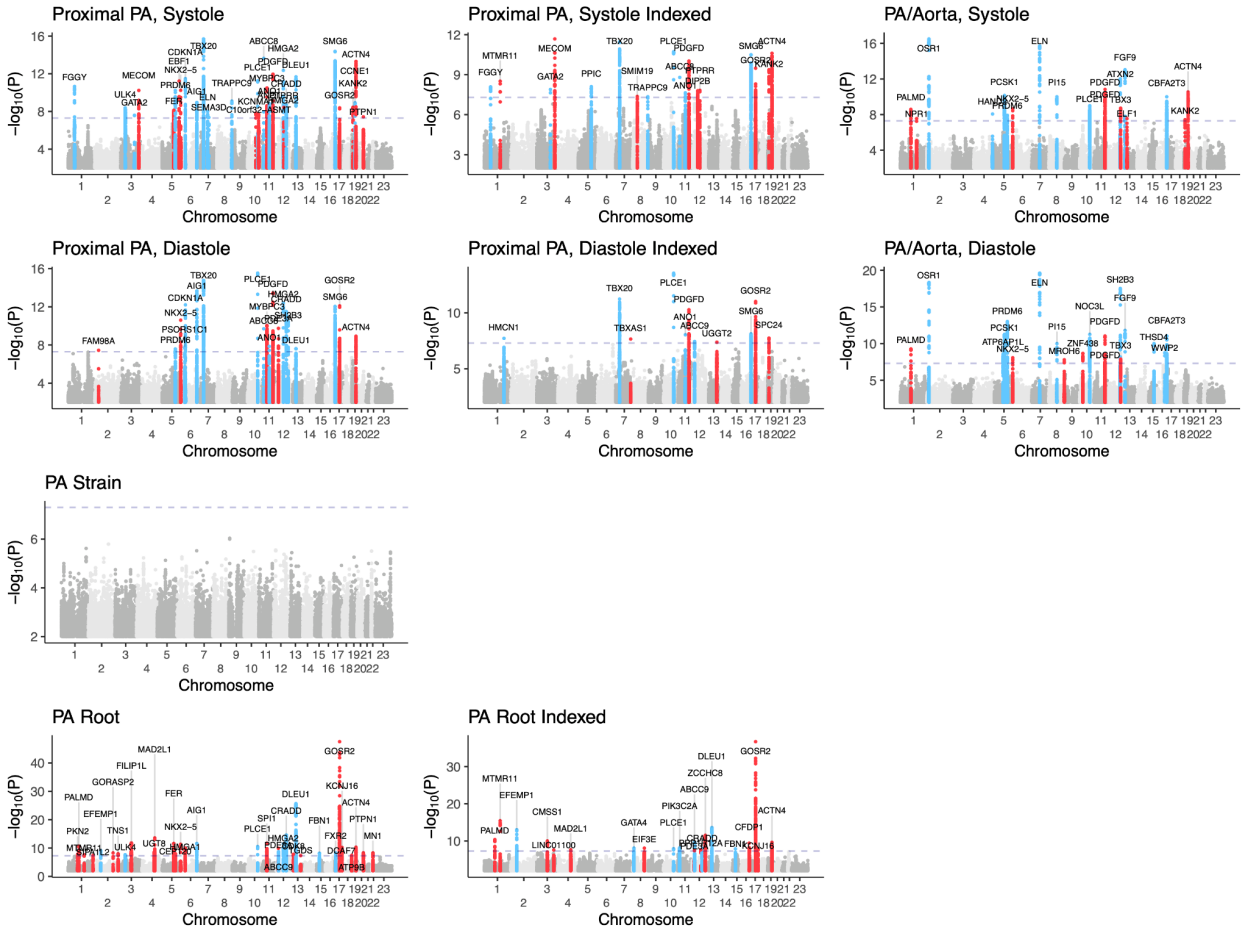

Manhattan plots are depicted for the outflow tract traits. Where relevant, the leftmost column contains the native trait, the middle column contains the body surface area indexed-trait, and the rightmost column contains the trait indexed to its left heart-equivalent. The **x axes** represent the chromosome and position. The X-chromosome is represented as “Chromosome 23.” The **y axes** represent the -$\log_{10}$(P), where P represents the BOLT-LMM association P value. Loci that contain SNPs with P < 5E-08 were labeled with the name of the nearest gene. These loci were colored blue if they were also associated with left heart phenotypes with P<5E-08, and otherwise were colored red.

Supplementary Figure 10: Loci significant after indexing on left heart traits

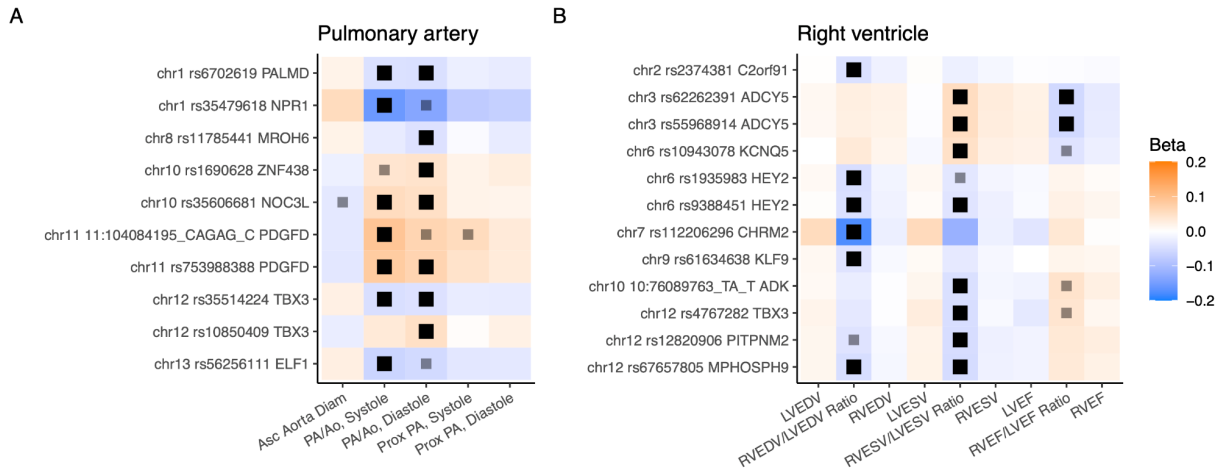

Each grid region represents the effect size (**Beta**) of the minor allele of the SNP (**y axis**) on the trait (**x axis**). The effect is represented by orange (increase) and blue (decrease). Black boxes within a grid region indicate that the association between the SNP and the trait has P < 5E-08; those with a gray box indicate P < 5E-06. P represents the BOLT-LMM association P value. “PA/Ao” is the ratio of the pulmonary artery diameter to the ascending aortic diameter. Exact P values are provided in **Supplementary Table 7** for traits with P < 5E-08, and in the summary statistics where P >= 5E-08. **Panel A**: SNPs associated with pulmonary artery phenotypes after indexing on aortic diameter. **Panel B**: SNPs associated with right ventricular phenotypes after indexing on their corresponding left ventricular measurement. Loci may be represented multiple times if the lead SNP differs between two traits (e.g., *TBX3*, the lead SNP for which differs between the pulmonary artery to aorta ratio in systole and in diastole).

Supplementary Figure 11: *BAG3* locus for RVESV and LVESV

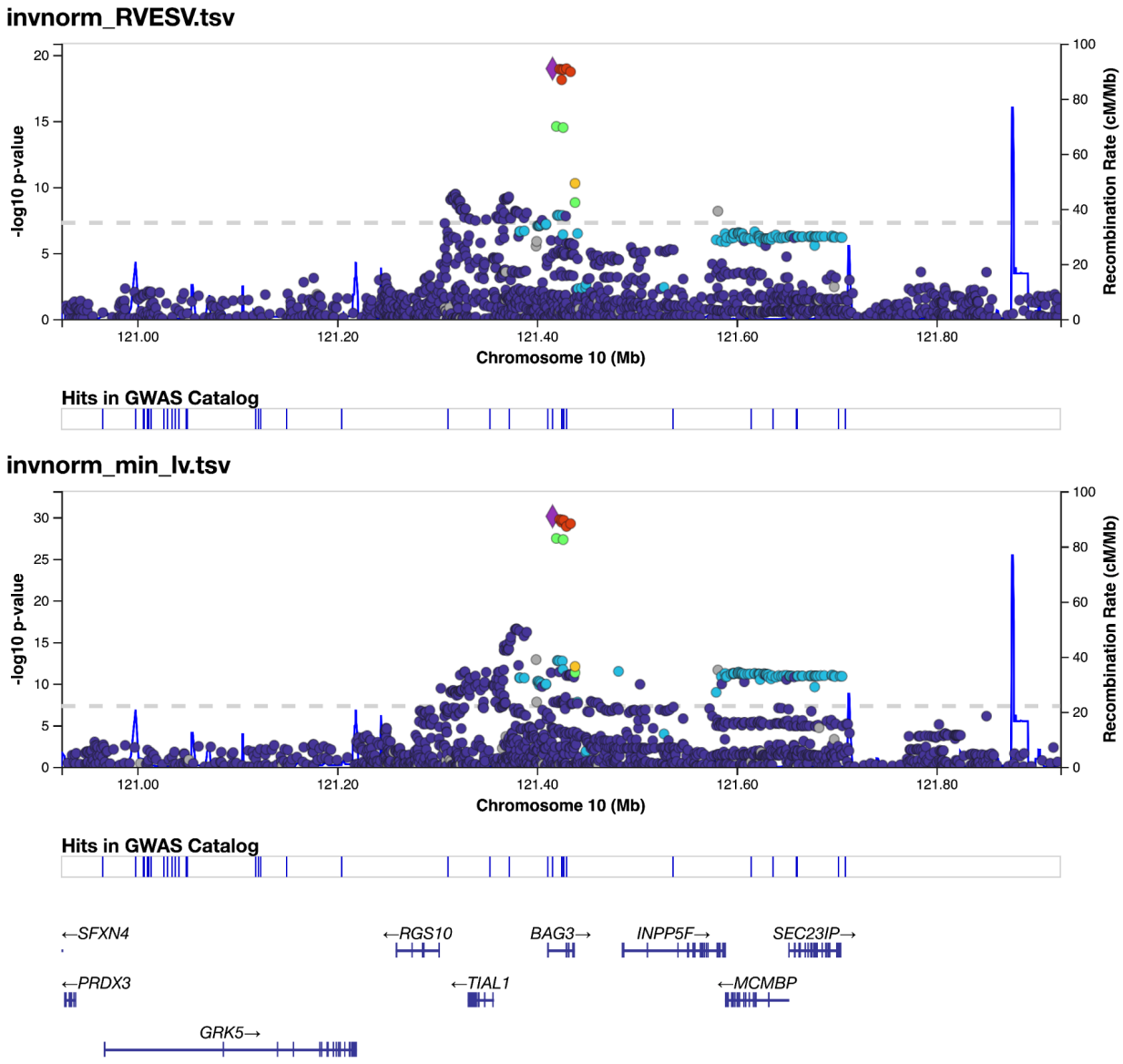

Supplementary Figure 12: *TTN* locus for RVESV and LVESV

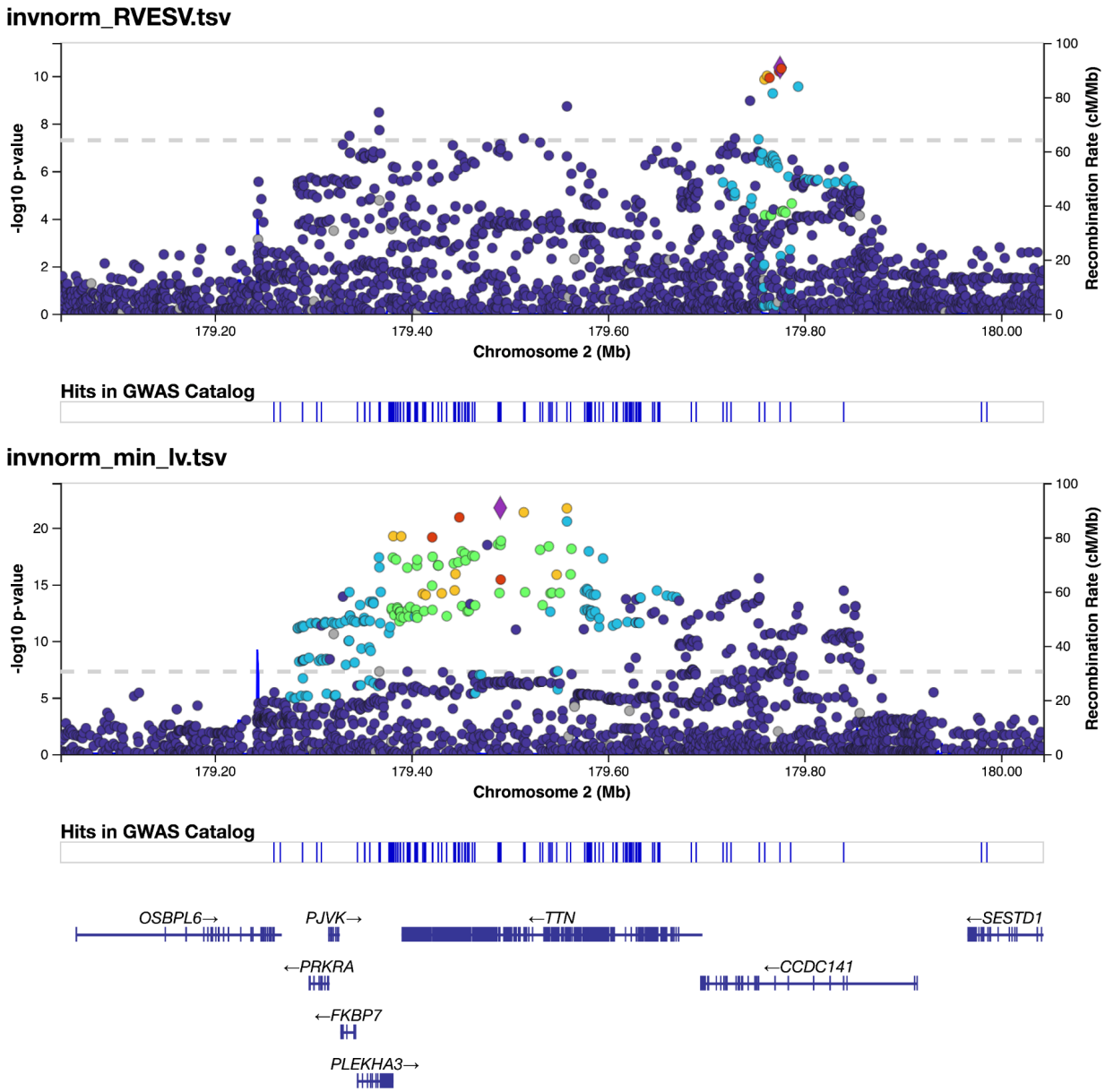

Supplementary Figure 13: *GATA4* locus for RVESV and LVESV

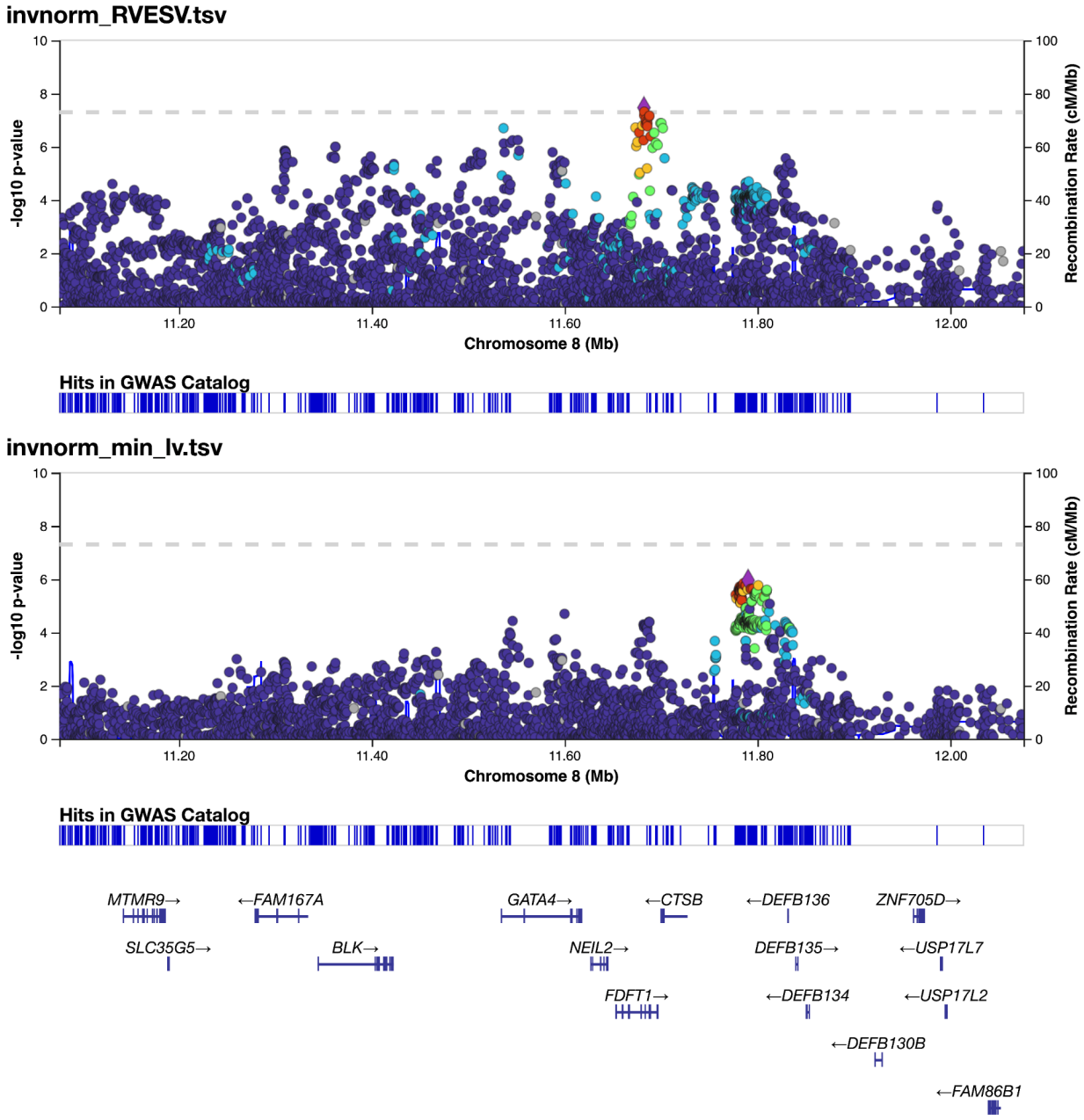

Supplementary Figure 14: *OBSCN* locus for RVESV and LVESV

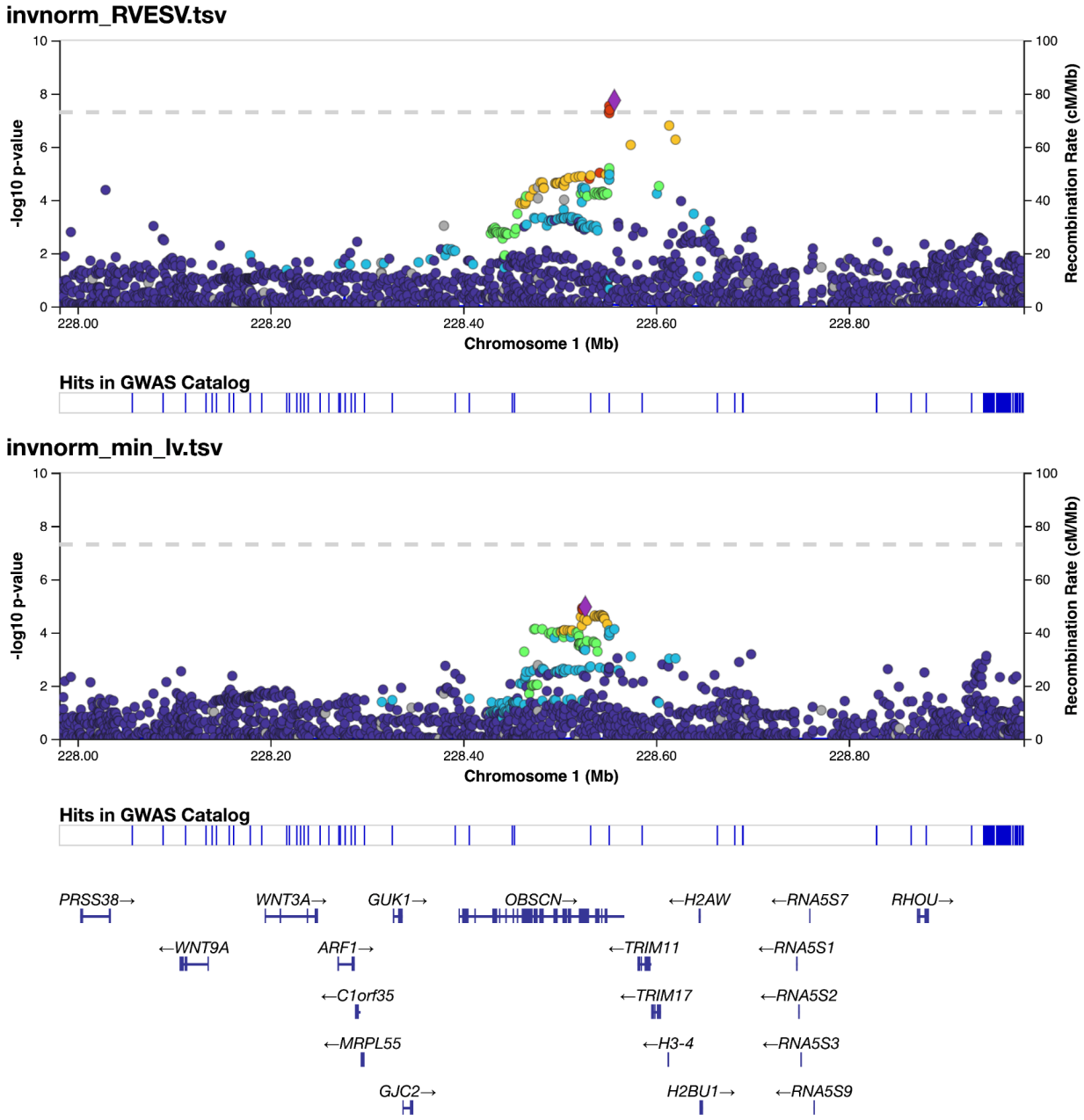

Supplementary Figure 15: *ADCY5* locus for RVESV/LVESV

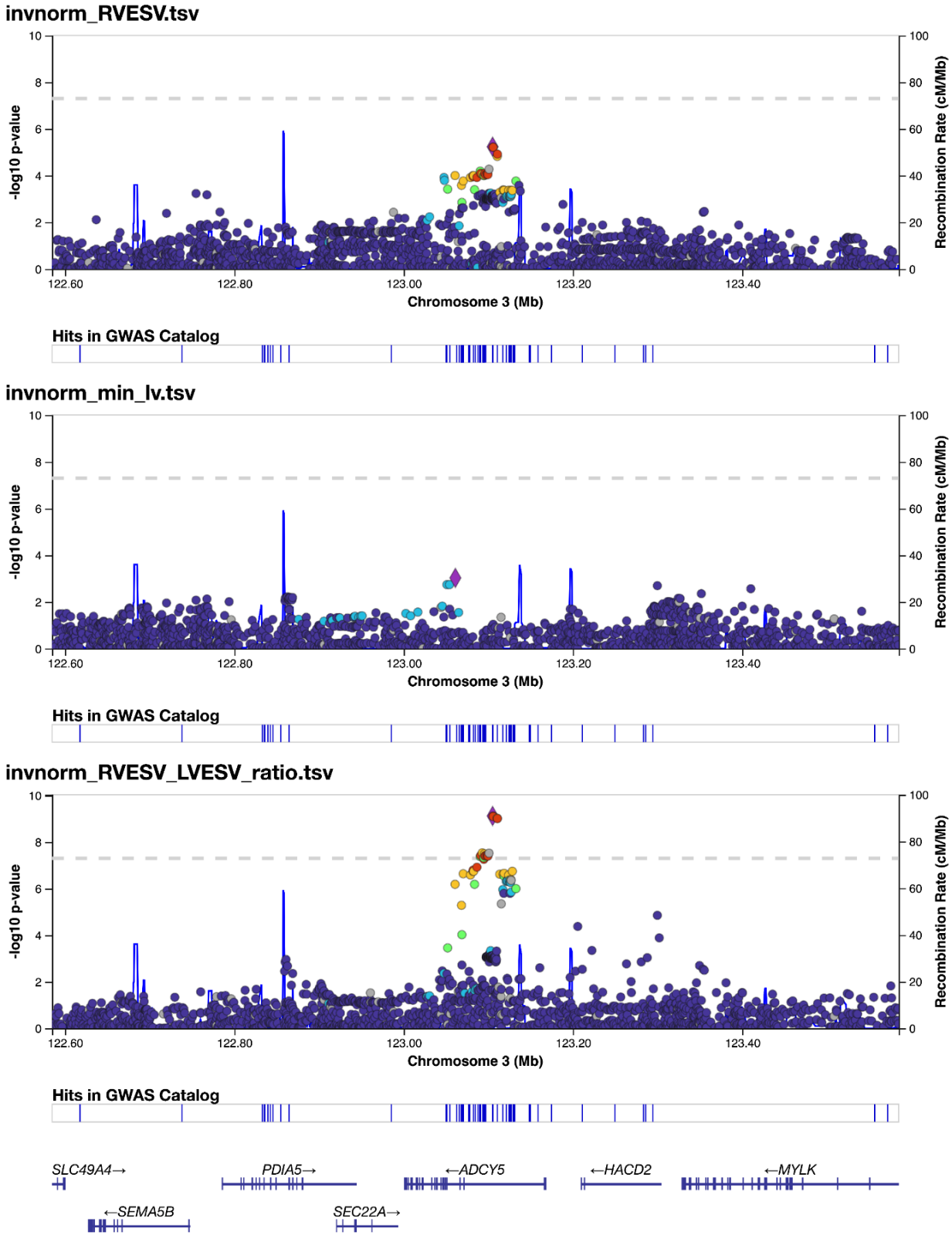

Supplementary Figure 16: Pulmonary artery GWAS locus external replication

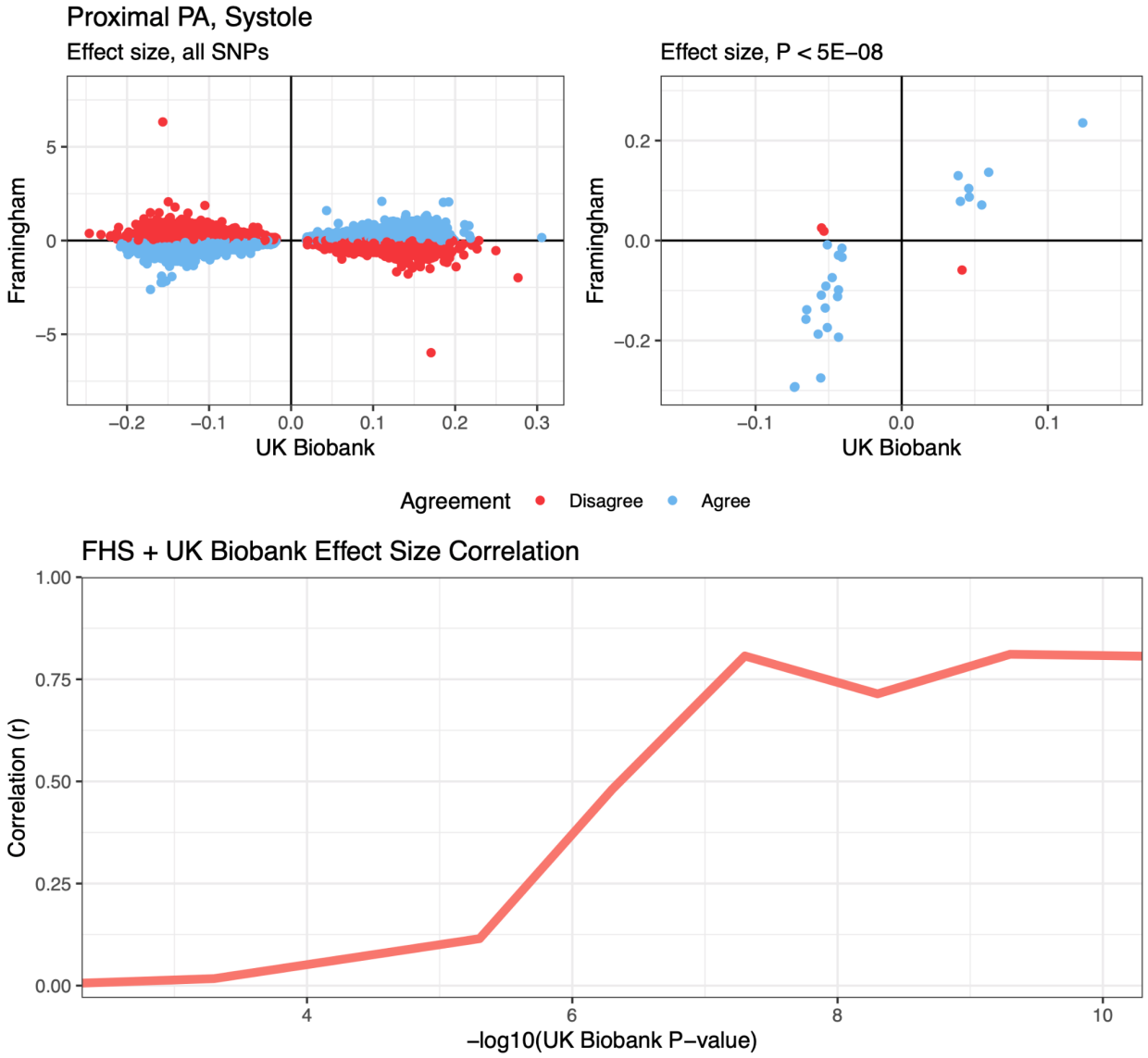

SNPs from the pulmonary artery diameter in systole GWAS were clumped based on in-sample LD within the UK Biobank using a linkage disequilibrium r^2 cutoff of 0.001 to identify independent signals. A lookup of the effect size of each SNP on pulmonary artery diameter in Framingham (FHS) was then conducted. **Top left panel**: Relationship between UK Biobank effect size (x axis) and FHS effect size (y axis). **Top right panel**: Same relationship, limiting SNPs to those with UK Biobank association P < 5E-08 (where P represents the BOLT-LMM association P value). Exact P values are available in **Supplementary Table 11**. **Bottom panel**: Correlation coefficient (y axis) between the FHS and UK Biobank SNP effect sizes for SNPs below the UK Biobank BOLT-LMM P value cutoff shown on the x axis.

Supplementary Figure 17: SNPs near *TBX5*/*TBX3*

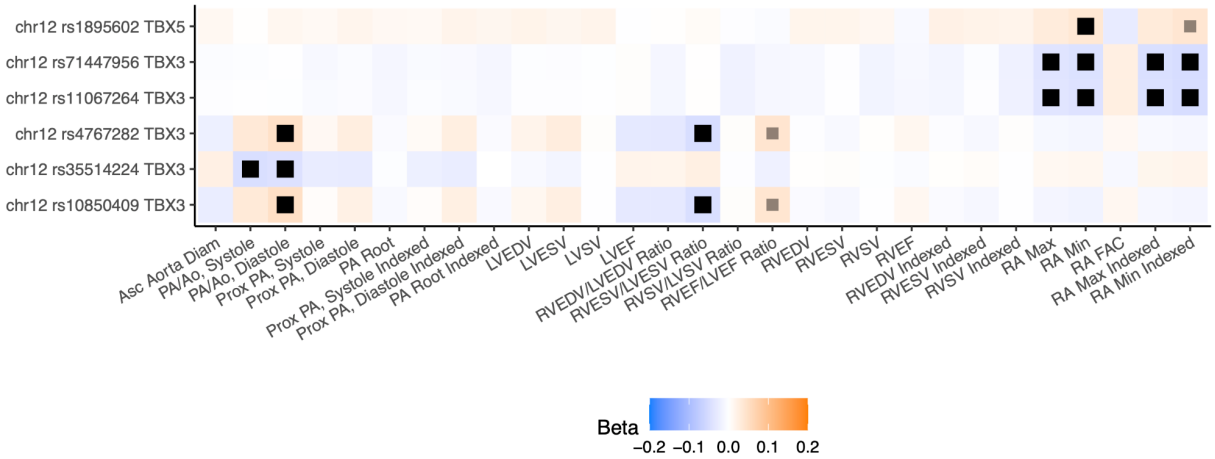

SNPs near *TBX5*/*TBX3*. Positioning on the y axis is based on genomic order. Color is based on effect direction. Black boxes indicate GWAS P value < 5E-08 from BOLT-LMM. Gray boxes indicate GWAS P value < 5E-06 from BOLT-LMM. Exact P values are provided in **Supplementary Table 7** for traits with P < 5E-08, and in the summary statistics where P >= 5E-08.

Supplementary Figure 18: Pulmonary artery TWAS

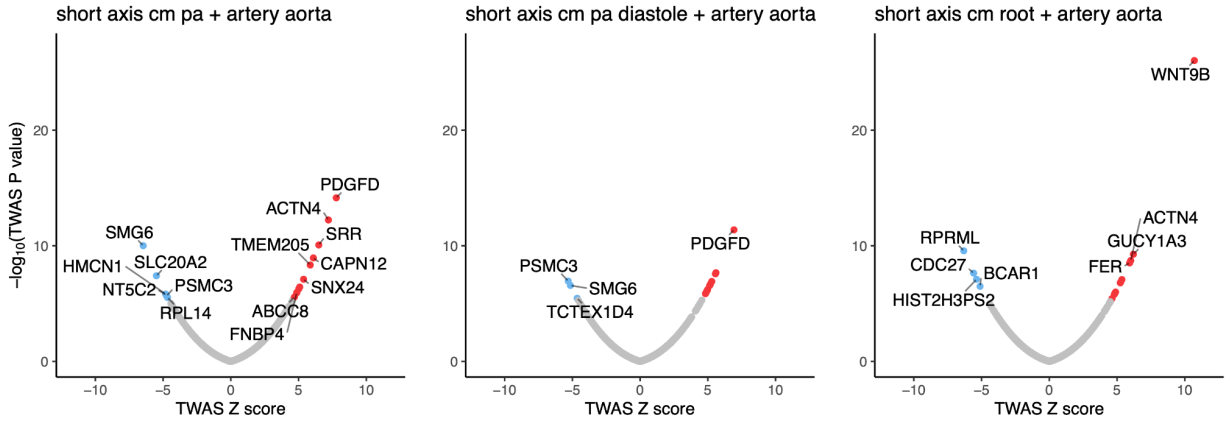

TWAS results for the pulmonary artery phenotypes (systole, **left**; diastole, **middle**; and the root, **right**), using the aorta as the derivation tissue for gene expression.

Supplementary Figure 19: Chamber-specific cell type enrichment

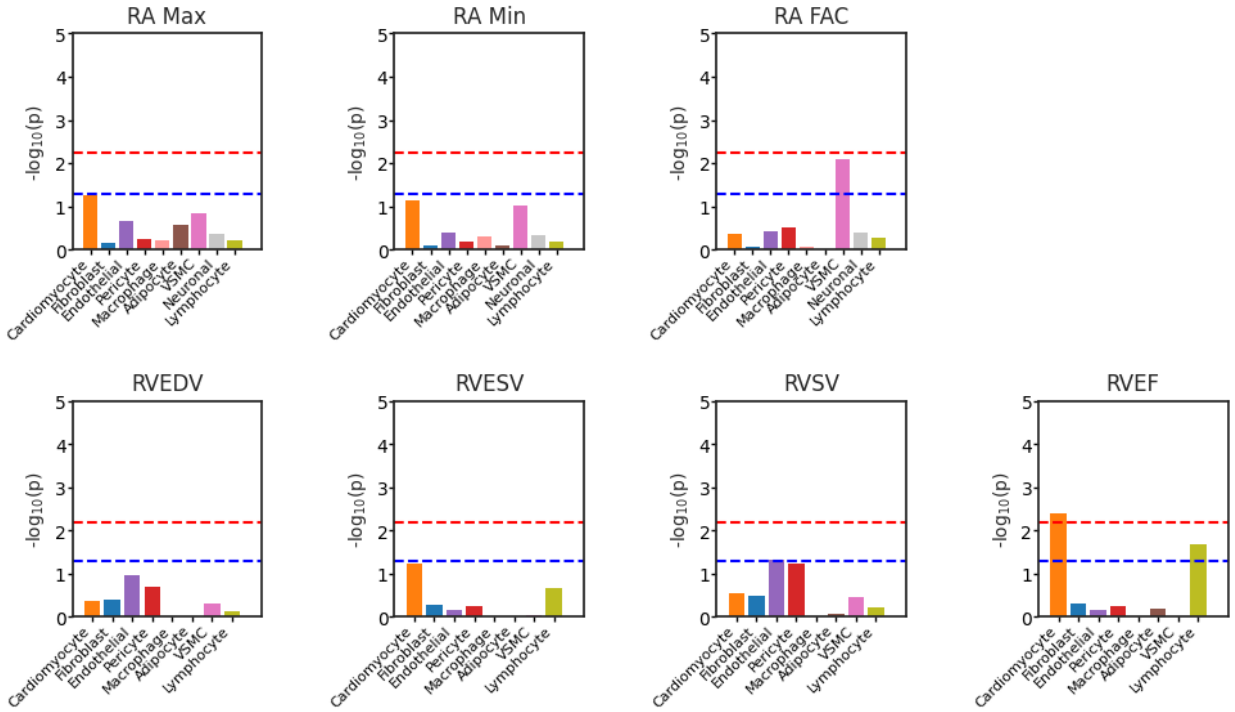

For the three primary right atrial phenotypes and four primary right ventricular phenotypes, stratified LD-score regression was performed. For the right atrial phenotypes, right atrial expression data was used, and for the right ventricular phenotypes, right ventricular expression data was used. The blue dashed line represents nominal significance while the red dashed line represents trait-wise significance.

Supplementary Figure 20: Gene sets enriched near GWAS loci

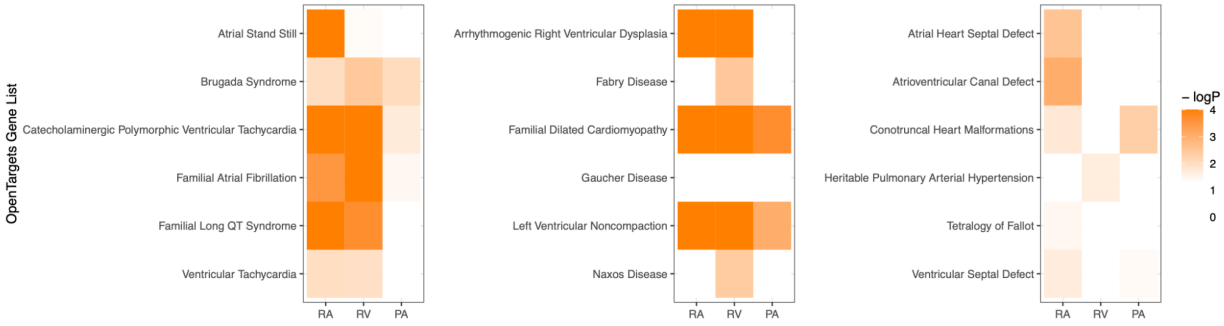

One-tailed permutation P values based on overlap between GWAS loci and OpenTargets gene sets for arrhythmias and channelopathies (**left panel**), myocardial diseases (**middle panel**), and conotruncal or atrioventricular canal abnormalities (**right panel**). RA: right atrium. RV: right ventricle. PA: pulmonary artery or root.

Supplementary Figure 21: *JUP* locus for RVESV and LVESV

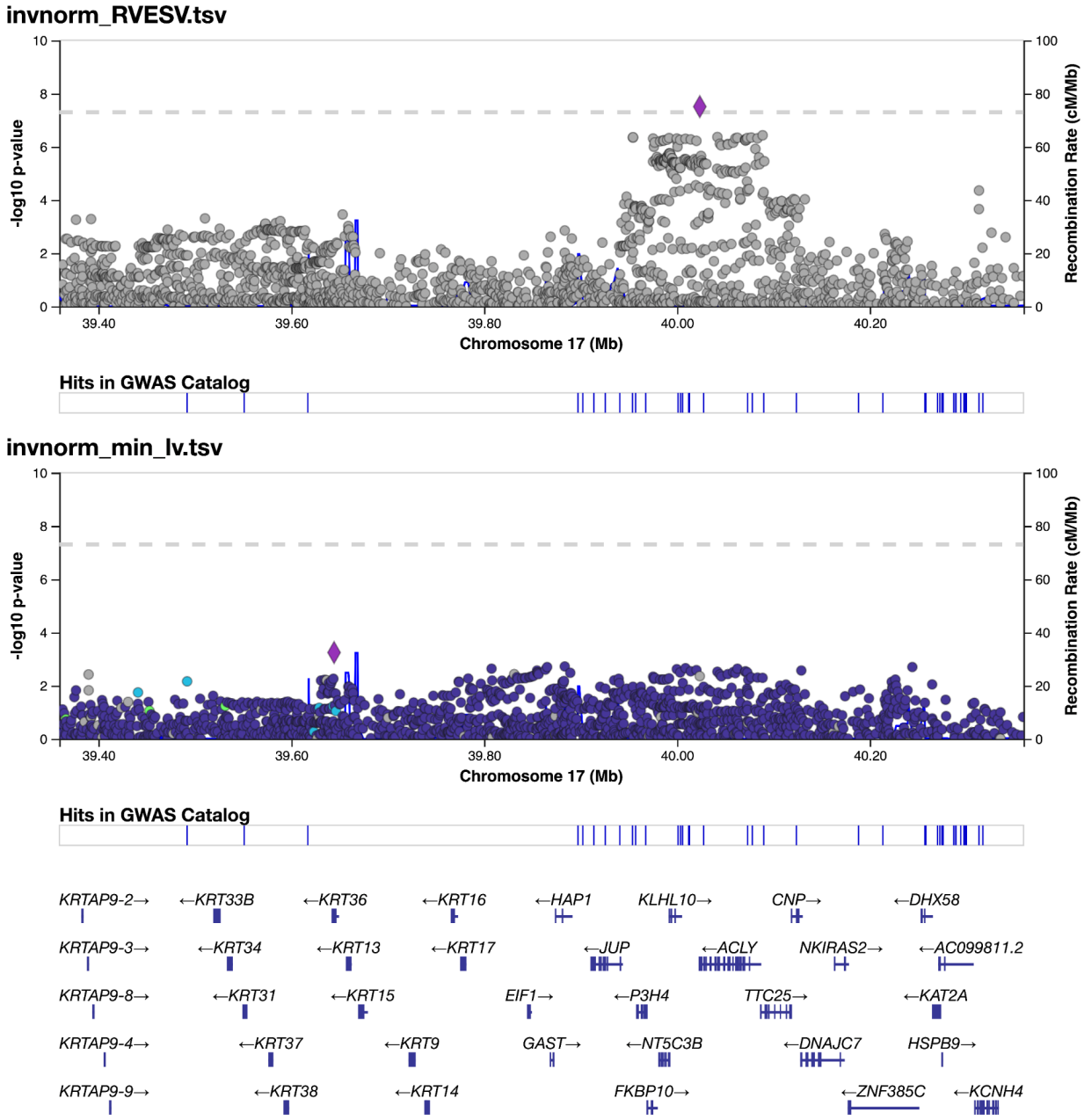

Supplementary Figure 22: Training set sample size

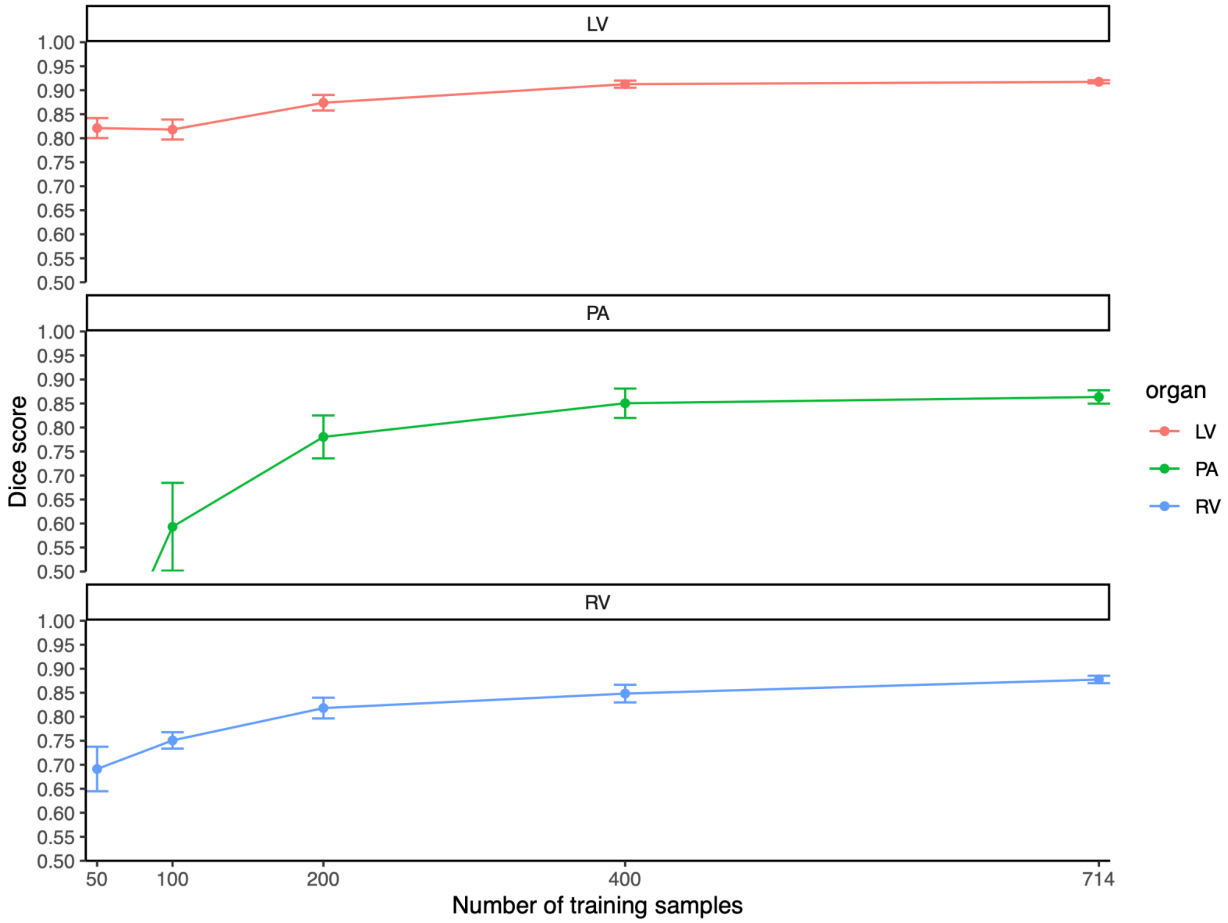

The short axis segmentation model was re-trained with between 50 and the full 714 training samples (**x axis**) to demonstrate the dependence of the Dice score (**y axis**) for the blood pools of the left ventricle (LV), the pulmonary artery (PA) and right ventricle (RV) on the number of training samples. The center point represents the mean Dice score, based on 5 replicates for each number of training samples, and the error bars represent one standard error above and below that value. The Dice score for the pulmonary artery blood pool with 50 training samples was below 0.5 and is not displayed.